Planetary and Space Science 209 (2021) 105356

Contents lists available at ScienceDirect

Planetary and Space Science

journal homepage: www.elsevier.com/locate/pss

A deep-ultraviolet Raman and Fluorescence spectral library of 62 minerals for the SHERLOC instrument onboard Mars 2020

Joseph Razzell Hollis [a,*], William Abbey [a], Luther W. Beegle [a], Rohit Bhartia [b], Bethany L. Ehlmann [c], Jasper Miura [c], Brian Monacelli [a], Kelsey Moore [a], Austin Nordman [a], Eva Scheller [c], Kyle Uckert [a], Yen-Hung Wu [a]

[a] NASA Jet Propulsion Laboratory, California Institute of Technology, Pasadena, CA, USA
[b] Photon Systems, Covina, CA, USA
[c] California Institute of Technology, Pasadena, CA, USA

ARTICLE INFO

Keywords:
Deep-ultraviolet Raman spectroscopy
Mars 2020
Mars
Mineralogy
SHERLOC

ABSTRACT

We report deep-ultraviolet (DUV) Raman spectra as measured by a SHERLOC analog instrument (248.6 nm excitation) for 92 samples representing 62 distinct minerals, including borates, carbonates, sulfates, phosphates, halides, metal oxides & hydroxides, silicates & phyllosilicates. We found that DUV Raman is capable of detecting the majority of these minerals, with major mineral peaks occurring at ~500, ~850, 950–1200, and ~3600 cm^{-1}, and that detection thresholds will be better for the SHERLOC flight instrument than the analog used in this study. Minerals can be classified (e.g., sulfate vs carbonate, or pyroxene vs olivine) based on the number of major peaks and their general positions. Identification of specific mineral phases is possible based on precise Raman peak positions, provided the difference between spectrally similar minerals is at least 10 cm^{-1} to overcome the estimated instrumental uncertainty of ±5 cm^{-1} for all peak positions reported in this study. A number of silicate minerals did not produce measurable Raman signal, and iron-rich minerals tend to be more difficult to detect due to significant UV absorption. Many Mars-relevant minerals expected to occur in Jezero crater should be detectable to SHERLOC even during short-exposure survey scans. This library will help inform the detection and identification of mineral phases in Martian samples using the SHERLOC instrument onboard the Mars 2020 *Perseverance* rover.

1. Introduction

On the 18th of February 2021, NASA's *Perseverance* rover landed in Jezero crater, Mars, and has begun surface science operations. The stated goals of the mission are to explore the astrobiologically relevant environment of Jezero, decipher its geological processes and history, assess biosignature preservation potential of the local geology, and collect and cache samples for eventual return to Earth [Mustard et al., 2013; Farley et al., 2020]. In order to achieve these goals, *Perseverance* is equipped with seven scientific instruments, one of which is called Scanning Habitable Environments with Raman and Luminescence of Organics and Chemicals (SHERLOC). SHERLOC is a compact deep ultraviolet (DUV) Raman and fluorescence spectrometer mounted on the turret at the end of the rover's robotic arm, designed to detect and characterize both organic material and mineralogy at sub-millimeter spatial resolutions on natural and abraded samples [Bhartia et al., 2021]. By scanning a 248.6 nm pulsed laser across a target surface and collecting any photons of Raman scattering and fluorescence emitted by near-surface material, SHERLOC will map organic and mineral composition at the microscopic scale to interrogate the geochemical history of rocks and regolith in Jezero crater.

Jezero crater is a 45 km diameter Noachian epoch impact structure on the northwest edge of Isidis Planitia. It was selected as the *Perseverance* landing site because orbiter-acquired imagery and visible/near-infrared spectral mapping suggest that it was the location of a paleolake and river system at a time when Mars was warmer, wetter, and might have been potentially habitable [Fassett and Head, 2005; Ehlmann et al., 2008a; Murchie et al., 2009; Schon et al., 2012; Williford et al., 2018; Stack et al., 2020]. The presence of a fluvial delta, lacustrine deposits, carbonates, and smectite clays indicate a complex geological history of

* Corresponding author. NASA Jet Propulsion Laboratory, 4800 Oak Grove Drive Pasadena, CA, 91104 USA.
E-mail address: hollis@jpl.nasa.gov (J. Razzell Hollis).

https://doi.org/10.1016/j.pss.2021.105356
Received 18 May 2021; Received in revised form 16 August 2021; Accepted 29 September 2021
Available online 20 October 2021

extensive aqueous alteration and significant geological diversity [Ehlmann *et al.*, 2008ab; Goudge et al., 2015; Horgan et al., 2020]. The crater floor consists of two primary lithologies, a light-toned unit enriched in smectite/carbonate/olivine and a dark-toned mafic unit [Ehlmann et al., 2008a; Ehlmann et al., 2011; Horgan et al., 2020]. The sedimentary deltaic deposits on the western edge of Jezero are comprised of clay- and carbonate-bearing material transported from the fluvial watershed, and as such may potentially preserve organic material and biosignatures from the broader Nili Fossae region [Ehlmann et al., 2008a; Ehlmann et al., 2009; Goudge et al., 2017; Hays et al., 2017]. A carbonate-bearing unit on the western margin of the crater floor is of great interest as a possible lacustrine shoreline deposit that could have preserved fossil textures and a record of organic material available in the aqueous environment of the paleolake [Flan nery et al., 2018; Horgan et al., 2020]. A detailed investigation of the mineralogy and stratigraphy of the floor, delta, and basin-marginal carbonates will be essential to properly constrain the geological history of Jezero crater and the habitability of ancient Mars, and provide essential context for samples that will be collected, cached, and eventually returned to Earth.

SHERLOC uses Raman spectroscopy to detect organic compounds and minerals based on the inelastic scattering generated by molecular vibrational modes, which are highly specific to chemical structure. The identification and classification of different materials can be achieved through analysis of the pattern of Raman peak positions detected [Long, 1977]. DUV Raman spectroscopy exploits the signal enhancement of high-energy excitation to significantly increase Raman scattering efficiencies, enabling reliable detection of chemical compounds at low laser power, avoiding damaging or consuming the sample [Asher, 1984; Asher, 1993; Beegle et al., 2015]. DUV fluorescence is a separate phenomenon, the direct absorption of 248.56 nm laser photons by molecules in the sample followed by emission of longer-wavelength photons, which tend to be spectrally broad and less specific to chemical structure. However, fluorescence is much easier to detect at very low concentrations due to its significantly higher quantum yield [Bhartia et al., 2012; Eshelman et al., 2019]. By using DUV excitation, SHERLOC can measure Raman scattering and fluorescence in different spectral ranges of a single spectrum: 250–275 nm (~200–4000 cm^{-1}) and 275–353 nm, respectively. This enables easier detection and analysis compared to visible excitation [Tarcea et al., 2008; Beegle et al., 2015; Razzell Hollis et al., 2021b]. SHERLOC was designed primarily to detect organic material, but is also capable of characterizing mineralogy based on the pattern and positions of Raman peaks between 800 and 4000 cm^{-1} that are generated by the internal vibrational modes of covalently bonded units within the mineral lattice [Griffit h, 1967]. The ability of SHERLOC to detect and distinguish minerals from one another, especially at the sub-millimeter scale, will be invaluable to interpreting the geological history of targets investigated by *Perseverance* in and around Jezero crater.

Given the diverse mineralogy we expect to find in Jezero crater, and the importance of identifying mineral targets with high biosignature preservation potential, we need to better constrain what types of minerals SHERLOC is capable of identifying. Because Raman peak positions and shapes may depend on the excitation wavelength due to Raman resonance effects, differences in penetration depth, and variations in background fluorescence, it is crucial that we measure and understand how mineral spectra appear at our operating wavelength of 248.56 nm, rather than relying on pre-existing Raman databases acquired using visible excitation (e.g. RRUFF). Furthermore, SHERLOC's mass and volume requirements lead to a unique optical design that means preliminary mineral characterizations done on other DUV Raman instruments may not be entirely representative in terms of detection thresholds or observed peak intensities and widths [Bhartia et al., 2021]. Spectra in this study were obtained using the SHERLOC Brassboard, a custom DUV spectrometer designed to be as optically similar to SHERLOC as possible while being able to operate under ambient temperature and pressure on Earth. Using optically similar instrumentation means that measured spectra are as close as is practical to what would be observed by SHERLOC on Mars, and can be used to better understand SHERLOC's capability to detect and identify minerals.

To help accurately identify minerals from SHERLOC spectra, we have collected a DUV spectral library of 62 natural and synthetic minerals inferred to be relevant to the geology of Jezero crater and the surrounding region [Ehlmann et al., 2008a,b; 2019; Goudge et al., 2015; Brown et al., 2020; Horgan et al., 2020; Scheller and Ehlmann, 2020]. We have included evaporitic and diagenetic minerals, such as carbonates, sulfates, borates, and halides, as well as mafic and felsic silicates, such as olivines, pyroxenes, quartz and phyllosilicate clays. Fig. 1 shows how the major peak positions of these different groups tend to appear at certain Raman shifts, the majority between 800 and 1800 cm^{-1} but with some additional peaks appearing at ~450 and 3000–3700 cm^{-1}, demonstrating how classification and identification of minerals can work. This library will enable the *Mar s 2020* science team to rapidly interpret some mineralogical aspects of SHERLOC spectra obtained during surface operations, and support tactical decision making regarding the caching of samples for eventual return to Earth [McLennan, 2011; Beaty et al., 2019].

2. Methods

Table 1 lists the 92 samples characterized in this study, representing 62 distinct minerals and rocks. Chemical formulas and sources for each sample are given where possible. The list of individual samples includes multiple suites that have been previously characterized in the literature using DUV Raman or other techniques [Ehlmann, 2010; McCollom et al., 2014; Thomas et al., 2018; Fox et al., 2021; Razzell Hollis et al., 2021a]. Each sample was named according to its form at the time of measurement (single crystal, rock, powder, or pellet). We also include any unique sample names or identifiers from previous studies in Table 1. Sample compositions have been previously verified using X-Ray Diffraction (XRD) or X-Ray Fluorescence (XRF).

2.1. Sample preparation

The majority of samples were natural minerals consisting of large single crystals, pieces of rock, or powdered material. All natural samples were previously identified using XRD (see referenced papers in Table 1). Crystal and rock samples were placed on a clean Al wafer, angled where necessary to ensure a flat surface was presented to the DUV spectrometer for even characterization. For powdered samples, a small quantity of powdered material was placed on a clean Al wafer and patted flat with a spatula to provide a relatively flat surface for characterization. Unless stated otherwise, pelleted samples were prepared by compressing powdered material under 9 metric tons of pressure to form a ~12 mm diameter solid pellet with a uniformly flat surface for characterization. The following mineral samples were comprised of synthetic material (see Table 1 for sources): nahcolite, iron(II) sulfate, magnesium sulfate, sodium sulfate, potassium bromide, magnesium chloride, calcium chloride, and ammonium chloride. Pelleted samples originally prepared for other studies are summarized in the following paragraphs.

Fourteen pelleted samples of various minerals (identified as "Mix#-O″) were originally prepared by Thomas et al. [2018] as part of a suite of calibration samples for the ChemCam laser-induced breakdown spectroscopy (LIBS) instrument onboard the Mars Science Laboratory rover. The "O" designation signifies the pure mineral endmember of each basalt-mineral mixture. Although the Mix7-O sample was originally described as being magnesite, subsequent XRD analysis has shown that it was actually dolomite. All Mix#-O samples consisted of 25 mm diameter pellets with a typical grain size of <250 μm. Areas exhibiting visible signs of LIBS damage were deliberately avoided when selecting surface areas to scan with the Brassboard instrument.

Four sulfate samples (identified as Natro#) were pellets made of synthetic mineral powders in the natroalunite-natrojarosite solid solution series with varying Al/Fe content [McCollom et al., 2014]. The Natro6

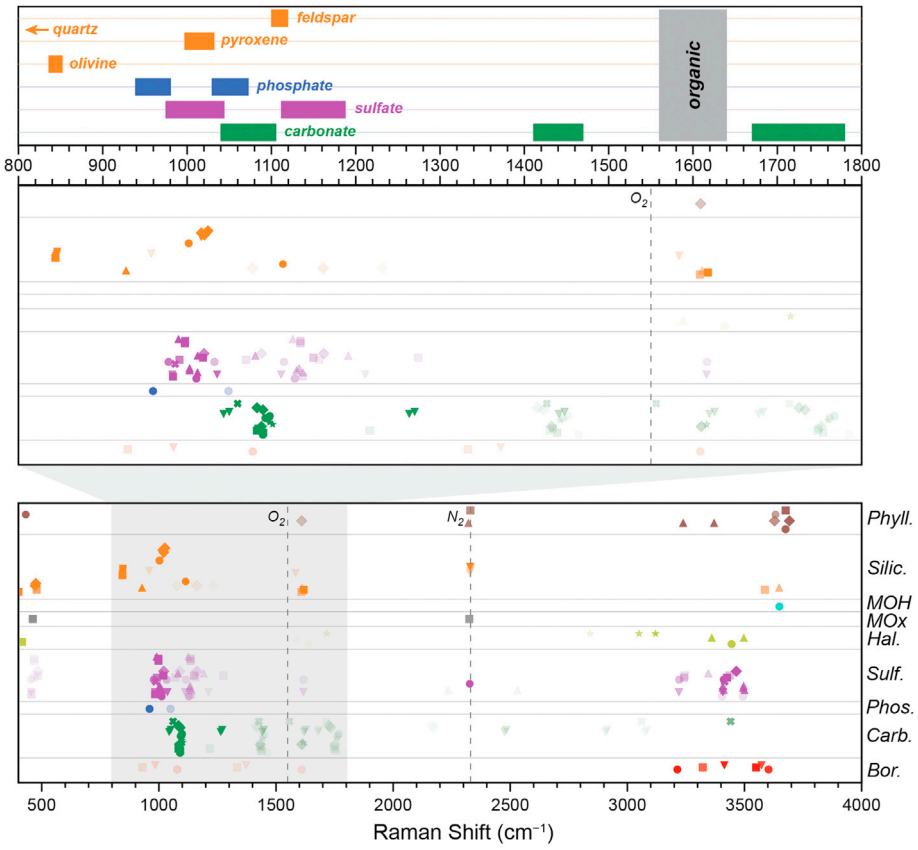

Fig. 1. Summary of Raman peak positions for 92 mineral samples, grouped and colored according to mineral class, showing how minerals can be classified by the pattern of Raman peak positions in the 800–1800 cm^{-1} region. Marker opacity indicates relative intensity of each peak. Bor: borate, Carb: carbonate, Phos: phosphate, Sulf: sulfate, Hal: halide, MOx: Metal oxide, MOH: metal hydroxide, Silic: silicate, Phyll: phyllosilicate.

sample had a relative Fe content of 0% (making it pure natroalunite), the Natro9 sample had a relative Fe content of 100% (pure natrojarosite), the Natro1 and Natro10 samples had intermediate compositions of 61% and 92% Fe respectively (and are referred to as natroalunite-natrojarosite).

Four olivine samples (named Pellets 1–4) were natural olivines, separated by picking from rocks and then crushed to particulates, with Forsterite (Fo) numbers of 88, 90, 82, and 1 respectively. They were previously characterized with infrared spectroscopy and electron microprobe [Buz and Ehlmann, 2017].

Six smectite samples (named Powder A, G, H, J, K, and N respectively) were synthetic mineral powders with intermediate compositions in the Fe(III)–Fe(II)–Al–Mg smectite solid solution series between the end-members of beidellite, montmorillonite, nontronite and saponite [Fox et al., 2021]. The A-J samples were exclusively Fe(III)-bearing smectites, while the K and N samples were predominantly Fe(II)-bearing at the time of preparation and initial DUV Raman measurements but may have oxidized during storage prior to Brassboard measurements. See Fox et al. [2021] for initial DUV Raman spectra plus detailed descriptions and characterization of each smectite.

2.2. DUV spectroscopy

All samples were measured by the SHERLOC Brassboard instrument at the NASA Jet Propulsion Laboratory. Like the flight instrument, the Brassboard instrument generates spatially-resolved spectral maps using laser-induced fluorescence and Raman signals, along with high-resolution microscopic images (10.1 μm/pixel) captured along the same narrow boresight. Both instruments use a pulsed NeCu 248.6-nm laser as the excitation source, firing 40 μs pulses at 80 Hz, focused to a nominal working distance of 48 mm using a custom *f*/7 objective lens. The focused spot is elliptical in shape, with an outer diameter of ~110 μm and an estimated illuminated area of ~7540 μm^2, delivering a relatively low energy dose of 30–45 mJ/cm^2 per laser pulse [Bhartia et al., 2021]. Fluorescence and Raman scattering photons from organics and minerals are collected using the same objective lens, and spectrally resolved with a single diffractive grating spectrograph with a wavelength range of 247–353 nm (roughly −200 to 12000 cm^{-1}). Rayleigh scattering and laser reflections are suppressed by a Semrock edge filter with an optical density >1 below 252 nm. Acquisition of a spectrum involves firing the DUV laser between 5 and 800 times, with the output of each DUV laser pulse recorded by a calibrated photodiode at the laser output. The accumulated Raman and fluorescence signal on the CCD was then read out vertically as a one-dimensional (1D) spectrum.

Spatial mapping is done using a motorized three-dimensional (3D) sample stage to translate the sample, compared to the flight instrument where the beam is rastered across the sample surface using a two-dimensional (2D) scanning mirror. An external Canon digital single-lens reflect (DSLR) camera with a 100 mm *f*2.8/L macro lens is aligned to the Brassboard field of view to provide high spatial resolution color images of each sample, analogous to the SHERLOC Wide-Angle Topographic Sensor for Operations and eNgineering (WATSON) subsystem camera onboard *Perseverance*.

Table 2 summarizes how the Brassboard spectral parameters compare to that of SHERLOC flight instrument. Instead of a 512 × 2048 pixel spectrometer CCD cooled by a phase-change material, the Brassboard uses a multi-stage thermoelectrically cooled (−54 °C) commercial Synapse Symphony II (Horiba) 512 × 2048 pixel CCD detector. The spectral pixel scale (the difference in spectral position for adjacent CCD channels, in cm^{-1}/pixel) was 10.73 cm^{-1} over the 400–4000 cm^{-1} range. Spectral resolution in the Raman region was estimated at 54.3 cm^{-1}, based on a measured full-width half maximum (FWHM) of 68.5 cm^{-1} for the 1580 cm^{-1} peak of highly oriented pyrolytic graphite (HOPG).

Table 1
Summary of samples characterized in this study, with their chemical compositions and sources. Sample references are given as follows:[1] Razzell Hollis et al. (2021a);[2] Thomas et al. (2018);[3] McCollom et al. (2014);[4] Ehlmann (2010);[5] Fox et al. (2021);[6] Buz and Ehlmann (2017). * indicates a synthetic mineral. Referenced works include additional source/synthesis information.

Mineral	Composition	Sample	Source and Identifying Information
Borates			
Colemanite	$Ca[B_3O_4(OH)_3]\cdot H_2O$	Powder[1]	Corkscrew Mine, Death Valley, California (*JPL Collection*). Minor inyoite ($Ca[B_3O_3(OH)_5]\cdot 4H_2O$)
Kernite	$Na_2[B_4O_6(OH)_2]\cdot 3H_2O$	Crystal[1]	Borax Mine, Boron, California (*JPL Collection*). Minor tincalconite ($Na_2[B_4O_5(OH)_4]\cdot 3H_2O$)
Ulexite	$NaCa[B_5O_6(OH)_6]\cdot 5H_2O$	Crystal[1]	Death Valley region, California *(JPL Collection)*
Carbonates			
Aragonite	$CaCO_3$ (orthorhombic)	Crystal	*JPL Collection*
Calcite	$CaCO_3$ (trigonal)	Crystal[1]	Santa Eulalia, Chihuahua, Mexico *(WARDS #49–5860)*
		Powder[1]	Santa Eulalia, Chihuahua, Mexico *(WARDS #49–5860)*
		Pellet[2]	ChemCam calibration target Mix2-O
Chalk	$CaCO_3$ (coccolithic)	Rock[1]	Dover, England *(WARDS #46–1449)*
Dolomite	$MgCa(CO_3)_2$	Crystal[1]	Butte, Montana *(WARDS #49–5871)*
		Powder[1]	Butte, Montana *(WARDS #49–5871)*
		Pellet[2]	ChemCam calibration target Mix7-O
Magnesite	$MgCO_3$	Crystal[1]	Brumado, Bahia, Brazil *(WARDS #49–5923)*
		Powder[1]	Brumado, Bahia, Brazil *(WARDS #49–5923)*
Nahcolite	$NaHCO_3$	Powder[1,*]	*Arm & Hammer Baking Soda*
		Pellet*	*Sigma-Aldrich (99.7%) (CAS #144-55-8)*
Rhodochrosite	$MnCO_3$	Crystal[1]	Sweet Home Mine, Alma, Colorado *(WARDS)*
		Powder[1]	Sweet Home Mine, Alma, Colorado *(WARDS)*
Siderite	$FeCO_3$	Crystal[1]	Ivigtut, Greenland *(WARDS #49–5911)*. Trace hematite (Fe_2O_3)
Trona	$Na_2CO_3\cdot NaHCO_3\cdot 2H_2O$	Powder[1,*]	*JPL Collection.* Minor thermonatrite ($Na_2CO_3\cdot H_2O$)
Phosphates			
Fluorapatite	$Ca_5(PO_4)_3F$	Crystal	Durango, Mexico *(WARDS #49–5855)*
Sulfates			
Anhydrite	$CaSO_4$	Powder[1]	Balmat, New York *(WARDS #46–0538)*. Minor (<15%) gypsum ($CaSO_4\cdot 2H_2O$)
Barite	$BaSO_4$	Powder[1,*]	*Wako Pure Chemicals #022-00425*
Epsomite	$MgSO_4\cdot 7H_2O$	Powder[1,*]	*CVS Epsom Salts*
Gypsum	$CaSO_4\cdot 2H_2O$	Crystal[1]	Tawas City, Michigan *(WARDS #46–3798)*
		Powder[1]	Tawas City, Michigan *(WARDS #46–3798)*
		Pellet[2]	ChemCam calibration target Mix13-O
Kieserite	$MgSO_4\cdot H_2O$	Powder*	*JPL Collection*
Melanterite	$FeSO_4\cdot 7H_2O$	Powder[1]	*JPL Collection.* Minor rozenite ($FeSO_4\cdot 4H_2O$) and trace szomolnokite ($FeSO_4\cdot H_2O$)
Natroalunite	$(Na_{0.82}H_3O^+_{0.18})Al_{2.69}(SO_4)_2(OH)_{5.07}(H_2O)_{0.93}$	Pellet 6[3,*]	Sample Natro6, Fe0
Natroalunite-Natrojarosite	$(Na_{0.91}H_3O^+_{0.09})(Al_{1.15}Fe_{1.79})(SO_4)_2(OH)_{5.82}(H_2O)_{0.18}$	Pellet 1[3,*]	Sample Natro1, Fe61
	$(Na_{0.86}H_3O^+_{0.14})(Al_{0.22}Fe_{2.51})(SO_4)_2(OH)_{5.19}(H_2O)_{0.81}$	Pellet 10[3,*]	Sample Natro10, Fe92
Natrojarosite	$(Na_{0.93}H_3O^+_{0.10})Fe_{2.96}(SO_4)_2(OH)_{5.88}(H_2O)_{0.12}$	Pellet 9[3,*]	Sample Natro9, Fe100
	$NaFe_3(SO_4)_2(OH)_6$	Powder[1]	*JPL Collection*
Thernardite	Na_2SO_4	Powder[1]	*JPL Collection*
Fe^{III} Sulfate	$Fe_2(SO_4)_3$	Pellet[2,*]	ChemCam calibration target Mix10-O
Fe^{II} Sulfate	$FeSO_4\cdot 7H_2O$	Pellet*	*Carolina Chemicals (99.7%) (CAS 7782-63-0)*
		Powder[1]	Tibet *(Caltech Collection)*
Mg Sulfate	$MgSO_4$	Pellet 1[2,*]	ChemCam calibration target Mix8-O
		Pellet 2*	*Macron Chemicals (CAS #7487-88-9)*
Na Sulfate	Na_2SO_4	Pellet 1[2,*]	ChemCam calibration target Mix11-O
		Pellet 2*	*Carolina Chemicals (99.5%) (CAS #7757-82-6)*
Halides			
Halite	NaCl	Crystal[1]	Window, Ontario, Canada *(WARDS #46–3823)*
		Pellet[2]	Chemcam calibration target Mix14-O
K Bromide	KBr	Pellet*	*Carolina Chemicals (99.5%) (CAS #7758-02-3)*
Mg Chloride	$MgCl_2$	Pellet*	*Sigma-Aldrich (98%)*
Ca Chloride	$CaCl_2$	Pellet*	*JT Baker (99.3%) (CAS #10043-52-4)*
Ammonium Chloride	NH_4Cl	Pellet*	*Macron Chemicals (CAS #12125-02-9)*
Oxides and Hydroxides			
Hematite	Fe_2O_3	Powder*	*JPL Collection*
Manganite	MnO(OH)	Rock	*JPL Collection*
Brucite	$Mg(OH)_2$	Pellet[2]	ChemCam calibration target Mix17-O
Silicates (by type)			
Silica phases			
Quartz	SiO_2	Powder[1]	Minas Gerais, Brazil *(WARDS #49–5886)*
		Pellet[2]	ChemCam calibration target Mix4-O
Opal	$SiO_2\cdot nH_2O$	Crystal	WARDS
		Pellet[2]	ChemCam calibration target Mix12-O

(*continued on next page*)

Table 1 (*continued*)

Mineral	Composition	Sample	Source and Identifying Information
Borates			
Glasses			
Basaltic Glass		Pellet[4]	Sample BAS-Gl, Hawaii. Also contains trace feldspar and pyroxene.
Pyroxenes			
Augite	$(Ca,Na)(Mg,Fe,Al,Ti)(Si,Al)_2O_6$	Powder	WARDS
		Pellet	Sample C20339 *(Caltech Collection),* contains minor fraction of other mineral
Diopside	$MgCaSi_2O_6$	Crystal	WARDS
		Pellet	Sample C7229 *(Caltech Collection)*
Enstatite	$MgSiO_3$	Crystal	WARDS
		Powder	WARDS
		Pellet	Sample C7758 *(Caltech Collection)*
Hedenbergite	$CaFeSi_2O_6$	Crystal	WARDS
		Pellet	Sample C16276 *(Caltech Collection)*
Plagioclases			
Albite	$NaAlSi_3O_8$	Crystal	WARDS
Bytownite	$(Ca_{0.7\text{-}0.9},Na_{0.3\text{-}0.1})Al(Al,Si)Si_2O_8$	Pellet	Sample C16630 *(Caltech Collection)*
Labradorite	$(Ca,Na)(Al,Si)_4O_8$	Powder	unknown
Olivines			
Fayalite	Fe_2SiO_4	Crystal	WARDS
Forsterite	Mg_2SiO_4	Crystal	WARDS
Olivine	$(Mg,Fe)_2SiO_4$	Pellet 1[6]	Sample OLV-SC, San Carlos, Fo88.
		Pellet 2[6]	Sample Polar Urals, Fo88.
		Pellet 3[6]	Sample Hualalai, Fo82
		Pellet 4[6]	Sample SP-568, Fo1
K-Feldspars			
Microcline	$KAlSi_3O_8$ (triclinic)	Crystal	WARDS
Orthoclase	$KAlSi_3O_8$ (monoclinic)	Crystal	WARDS
Other Silicates			
Epidote	$Ca_2Fe_{2.25}Al_{0.75}(SiO_4)_3(OH)$	Pellet[2]	ChemCam calibration target Mix20-O
Topaz	$Al_2SiO_4(F,OH)_2$	Pellet[2]	ChemCam calibration target Mix21-O
Phyllosilicates			
Clays			
Chlorite	$(Mg,Fe^{2+})_5Al(Si_3Al)O_{10}(OH)_8$	Pellet	Sample CCa-2 (*Clay Mineral Society standard*)
Illite	$(K,H_3O)(Al,Mg,Fe)_2(Si,Al)_4O_{10}$ $[(OH)_2,H_2O]$	Pellet	Sample IMF-2 (*Clay Mineral Society standard*)
Kaolinite	$Al_2Si_2O_5(OH)_4$	Powder	WARDS
Montmorillonite	$(Na,Ca)_{0.33}(Al,Mg)_2(Si_4O_{10})(OH)_2{\cdot}nH_2O$	Powder	WARDS
Smectite	$Ca_{0.37}Na_{0.10}[Fe^{III}_{1.68}Mg_{0.40}][Si_{3.32}Al_{0.51}Fe^{III}_{0.17}]O_{10}(OH)_2$	Powder A[5,*]	
	$Ca_{0.24}[Fe^{III}_{0.69}Mg_{1.12}Al_{0.52}][Si_{3.66}Al_{0.34}]O_{10}(OH)_2$	Powder G[5,*]	
	$Ca_{0.39}[Fe^{III}_{0.68}Mg_{1.75}Al_{0.02}][Si_{3.60}Al_{0.40}]O_{10}(OH)_2$	Powder H[5,*]	
	$Ca_{0.37}[Fe^{III}_{0.27}Mg_{2.31}Al_{0.08}][Si_{3.60}Al_{0.40}]O_{10}(OH)_2$	Powder J[5,*]	
	$Ca_{0.23}[Fe^{II}_{2.23}Fe^{III}_{0.28}Al_{0.26}Mg_{0.12}][Si_{3.51}Al_{0.49}]O_{10}(OH)_2$	Powder K[5,*]	
	$Ca_{0.27}Na_{0.08}[Fe^{II}_{0.80}Fe^{III}_{0.09}Al_{1.29}Mg_{0.10}][Si_{3.54}Al_{0.46}]$ $O_{10}(OH)_2$	Powder N[5,*]	
Micas			
Biotite	$K(Mg,Fe)_3(AlSi_3O_{10})(F,OH)_2$	Crystal	WARDS
Muscovite	$KAl_2(AlSi_3O_{10})(F,OH)_2$	Crystal	*JPL Collection*
		Pellet[2]	ChemCam calibration target Mix18-O
Serpentines			
Antigorite	$(Mg,Fe)_3Si_2O_5(OH)_4$	Pellet	Sample C11456 *(Caltech Collection)*
Serpentine	$(Mg,Fe)_3Si_2O_5(OH)_4$	Pellet[2]	ChemCam calibration target Mix19-O
Serpentinite	Rock with $(Mg,Fe)_3Si_2O_5(OH)_4$	Rock	WARDS

Table 2
A summary of key instrument parameters for SHERLOC and Brassboard instruments. **a)** Pulse energy at the target was estimated for SHERLOC at start of mission, under 25 A of driving current, and for the Brassboard under 15 A. **b)** Spectral resolution was determined from the FWHM of a typical Raman peak, that of HOPG. **c)** Spectral pixel scale (cm^{-1}/pixel) was calculated for the Raman region, 400–4000 cm^{-1}.

Instrument	CCD Temp.	Pulse Energy[a]	Spectral Range	Spectral Resolution[b]		Spectral Pixel Scale[c]	
	(°C)	(μJ)	(nm)	(nm)	(cm^{-1})	(nm)	(cm^{-1})
SHERLOC	−28	~9.0	249.9–353.6	0.270	40.3	0.0648	10.49
Brassboard	−54	2.84 ± 0.37	246.8–354.7	0.363	54.3	0.0663	10.73

Brassboard spectral calibration was based on fitting a quadratic function to the secondary laser line at 252.93 nm and the reported peak positions of three Raman standards: acetonitrile, powdered calcite, and HOPG; which occur between 919 and 2942 cm^{-1} (254.37–268.17 nm). The mean absolute error of the calibrated Raman peak positions with respect to their literature values was 2.7 ± 1.6 cm^{-1} (≈0.018 ± 0.010 nm). The spectral calibration in the fluorescence region (275–353 nm) was validated using the emission lines of an Hg arc lamp,

which showed that the mean absolute error of the calibration increases considerably with wavelength beyond the calibrated range, averaging 0.38 ± 0.22 nm between 275 and 310 nm, and 1.24 ± 0.27 nm between 310 and 355 nm (see Fig. S2).

The off-axis optical design of both instruments causes the projection of the spectrum to curve across the CCD, referred to as a 'spectral smile' (see Fig. S3 and Uckert et al., 2021). In order to avoid disruptive levels of dark noise in the Raman region that would result from integrating over the full height of the CCD, both instruments must read out data for the Raman and fluorescence regions separately using different vertical binning ranges. The SHERLOC onboard flight software is capable of reading each region independently from a single acquisition [Bhartia et al., 2021]. The Brassboard instrument emulates this by reading the Raman region and the fluorescence region of the CCD in two separate scans, which are then trimmed and combined to produce a full spectrum (as shown in Fig. S4).

To encompass the full range of exposure durations and energies that may be used in SHERLOC activities, each mineral sample was scanned multiple times with the Brassboard instrument at different laser settings, between 5 and 800 pulses per point (approximately equivalent to a total laser energy of 20–3000 μJ, or 0.26–30 J/cm^2). Each mineral sample was measured using an automated sequence of 6 scans at different laser settings. Each scan recorded 25 individual spectra in a 5 × 5 grid with 150 μm spacing (750 × 750 μm), and was done in a different location to minimize any photochemical damage caused by cumulative exposure to the DUV laser. The sequence of laser settings used were 5/25/100/400/800 laser pulses per point with the laser power supply (LPS) providing 20 A of current at 375 V, followed by a final scan of 800 pulses per point at 15 A and 375 V. The output energy of each laser pulse during each scan was recorded by a photodiode at the laser output, calibrated to the energy received at the sample. The average pulse energy was 2.84 ± 0.37 μJ/pulse at 15 A and 4.15 ± 0.38 μJ/pulse at 20 A. To reduce the total measurement time, the fluorescence region was only recorded once per mineral sample, at 100 laser pulses and 20 A. Images were taken before and after each scan, and no visible signs of laser-induced photo-damage were observed for any sample.

2.3. DUV data processing

All spectra were processed using in-house Python scripts utilizing Numpy [Van de Walt et al., 2011], SciPy [Jones et al., 2001], and LMFIT [Newville et al., 2014] packages. Each scan was processed in the following steps, which are visualized in Fig. S4: 1) individual spectra in the scan were rescaled to account for intensity changes resulting from variations in laser output, by multiplying each spectrum's intensity by a normalization factor equal to the total laser energy recorded during acquisition of that spectrum divided by the maximum laser energy recorded in the scan. 2) Cosmic rays were automatically identified as outliers in the distribution of intensity values in each CCD channel and replaced by the average value of adjacent spectral points [Uckert et al., 2019]. 3) Because this spectral library required measurement of nominally homogenous samples, outlier spectra were removed automatically, defined as >10% of the spectrum being >2 standard deviations from the average, followed by recalculation of the average and standard deviation using remaining spectra. 4) For duplex scans that recorded both the Raman and fluorescence regions of the CCD, the average Raman and average fluorescence values were added together, after trimming to remove dark noise from non-read regions. 5) Background intensity was removed from the Raman region of the averaged spectrum by subtraction of a polynomial baseline between 0 and 4000 cm^{-1}. The baseline was fitted to a set of points at Raman shifts that were free of Raman peaks, specific to each mineral or its class, and the fit was optimized by linear least squares regression. For some samples a second baseline fit and subtraction was required to ensure a clean background removal. 6) The baselined spectrum was then normalized, dividing intensity values by the maximum found between 400 and 4000 cm^{-1}, ignoring the 600–800 cm^{-1} region obscured by a NeCu laser emission line at ~695 cm^{-1}.7) Raman peak positions and intensities were determined by dividing the spectrum into sections and fitting each peak with a Gaussian function, with multiple functions used for overlapping peaks.

3. Results and discussion

3.1. Brassboard vs SHERLOC

The Brassboard instrument is designed to be a terrestrial analog for the SHERLOC flight instrument onboard *Perseverance*, utilizing a similar optical path and components to ensure the output is as equivalent as possible to SHERLOC measurements during the mission. Both instruments measure similar wavelength ranges from ~250 to ~355 nm, equivalent to a Raman shift range of ~200–~12000 cm^{-1} [Bhartia et al., 2021; Uckert et al., 2021]. The 250–252.3 nm (200–600 cm^{-1}) region is attenuated to <10% signal by the instrumental edge filter – meaning that only exceptionally strong Raman peaks can be observed – while the 252.3–253.3 nm (600–750 cm^{-1}) region is obscured by a secondary laser emission line at 252.93 nm (~695 cm^{-1}).

Unlike SHERLOC, the Brassboard instrument is designed to operate under Earth ambient conditions, leading to some differences in instrumental parameters (summarized in Table 2). These parameters were assessed by measuring the spectrum for a DUV Raman intensity standard of HOPG, an effectively planar source of Raman scattering with a single Raman peak at ~1580 cm^{-1}, with the results shown in Table 3. The ability of SHERLOC and the Brassboard to resolve and identify the positions of any Raman peaks is measured by two key parameters: spectral pixel scale (the difference between adjacent points in a spectrum) and spectral resolution (the minimum separation needed to resolve two overlapping peaks). Spectral pixel scale represents how accurately the position of individual peaks may be determined, and SHERLOC and the Brassboard have similar pixel scales of ~10.5 cm^{-1} (~0.065 nm) per pixel in the Raman region. Gaussian fitting can refine peak positions to sub-pixel scales (±1 cm^{-1}), when combined with the ±3 cm^{-1} uncertainty for the spectral calibration, suggests that all measured peak positions in this study have a minimum uncertainty of ±4 cm^{-1}. We assessed the reliability of the calibration by comparing observed Raman peak positions to literature values for 32 peaks across 10 samples of calcite, gypsum, fluorapatite, quartz, and HOPG [Krishnamurti, 1958; Gunasekaran et al., 2006; Brotton and Kaiser, 2013; Montagnac et al., 2013; De La Pierre et al., 2014; Litasov and Podgornykh, 2017]. The average discrepancy across the range ~470–~3500 cm^{-1} (251.52–272.27 nm) was +0.3 cm^{-1} with a standard deviation of ±4.3 cm^{-1}, consistent with the estimated uncertainty of our calibration (see Table S1 and Fig. S5 for more detail). We found that the calibration was most accurate at ~1200 cm^{-1} (256.22 nm), and least accurate at 470 cm^{-1} (251.52 nm) due to extrapolation of the spectral calibration function in the edge-filtered region <1000 cm^{-1}. We conclude that the unique design of SHERLOC (and the Brassboard) does not lead to significant systematic errors that cannot be accounted for by calibration, but that all measured Raman peak positions come with an estimated uncertainty of ±5 cm^{-1} due to random error, which may impact our ability to distinguish minerals that exhibit similar spectra with only small variations in peak position.

Spectral resolution indicates how far apart two overlapping peaks must be if they are to be distinguishable from one another, and is related to how broad a given peak appears on each instrument. Based on the FWHM of HOPG as measured by each instrument (68.5 cm^{-1} on the Brassboard, 50.9 cm^{-1} on SHERLOC), the Brassboard resolution was calculated to be 54 cm^{-1} (0.363 nm) in the Raman region, versus 40 cm^{-1} (0.270 nm) for SHERLOC [Bhartia et al., 2021]. This suggests that SHERLOC will be better able to resolve overlapping peaks at narrower separations where the Brassboard may only detect a single, convoluted peak at an intermediate position, which may impact the identification of certain minerals that are known to produce distinctive

Table 3
Raman peak properties and signal-to-noise ratios (SNRs) as measured by SHERLOC (under simulated Martian ambient conditions) and Brassboard instruments (under Earth ambient conditions) for the 1580 cm^{-1} peak of HOPG, averaged over a 25 point scan. Peak intensity and full-width half maximum (FWHM) were derived by Gaussian fitting after background subtraction. Noise was estimated by the standard deviation of intensity values in the peak-free region between 2000 and 2100 cm^{-1}.

Instrument	Pulses	Pulse Energy (μJ)	Total Energy (μJ)	FWHM (cm^{-1})	Intensity (counts)	Noise (counts)	Signal:Noise Ratio	Pulse-Weighted SNR	Energy-Weighted SNR
SHERLOC	448	~9	~4000	33.0	3909	5.5	716	1.60	0.179
Brassboard	800	3.4	2700	42.4	897	4.3	208	0.26	0.077
S/B Ratio		*2.6x*	*1.5x*	*0.78x*	*4.4x*	*1.3x*	*3.4x*	*6.2x*	*2.3x*

spectra containing doublets (such as olivine).

We also expect that SHERLOC, operating on Mars, will differ from the Brassboard in terms of measured signal (Raman intensity yielded from a sample under given conditions) and sensitivity (the ability of the instrument to distinguish that signal against background noise). SHERLOC employs a more powerful laser than the Brassboard, generating roughly 9 μJ of incident laser energy per pulse at the start of mission compared to a measured output of 3.4 μJ/pulse for the Brassboard [Bhartia et al., 2021]. Based on the values summarized in Table 3, we estimate that SHERLOC – at the start of the surface mission –will be roughly 6x more sensitive than the Brassboard for the same number of laser pulses, under typical operating conditions. Even after accounting for the difference in energy output per pulse, SHERLOC is still about 2x more sensitive than the Brassboard due to better optical throughput and component variabilities. As such, with similar spectral acquisition parameters, the SNR of spectra obtained on the Brassboard should be considered the lower limit of SHERLOC's capabilities. Given the calculated difference in sensitivity, the 25-point average spectra shown in this paper are approximately equivalent to a single-point spectrum acquired on SHERLOC under similar conditions. As a result, some minerals that do not show detectable Raman scattering in this paper may still be detectable to SHERLOC through spatial averaging of multiple points.

Fig. 2a shows how a typical mineral (single-crystal calcite) appears when measured by SHERLOC and the Brassboard under their respective operating conditions. The SHERLOC spectrum was a single measurement acquired with 50 laser pulses, while the Brassboard spectrum was the average of 25 points acquired with 100 laser pulses per point. The spectra are fairly typical of the minerals we have studied, with the strongest signal coming from Raman peaks around 255–260 nm (1000–1800 cm^{-1}), though the SHERLOC test sample does show two broad fluorescence features at 270–310 and 310–350 nm that was not observed in the Brassboard test sample. Fig. 2a is an excellent demonstration of how Raman and fluorescence peaks typically appear in separate spectral regions, ~254–275 nm (800–4000 cm^{-1}) and ~275–355 nm respectively.

Fig. 2b shows that both spectra exhibited a single major Raman peak at 1085 cm^{-1} (255.47 nm), plus two minor Raman peaks at 1432 and 1748 cm^{-1} (257.73 and 259.86 nm) that are relatively low intensity. All three peaks are assigned to the *internal vibrational modes* (ν_i) of the covalently-bonded carbonate oxyanion [Griffith, 1969], and fitted positions were within 2 cm^{-1} between SHERLOC and Brassboard measurements. While lower frequency *lattice modes* are reported for many minerals including calcite, they tend to appear at <300 cm^{-1} and thus fall outside SHERLOC's spectral range [Griffith, 1969; Litasov and Podgornykh, 2017; Bhartia et al., 2021].

The spectra in Fig. 2 are not identical because, unlike SHERLOC, the Brassboard is designed to operate under Earth ambient conditions rather than Mars ambient, leading to some necessary differences in key

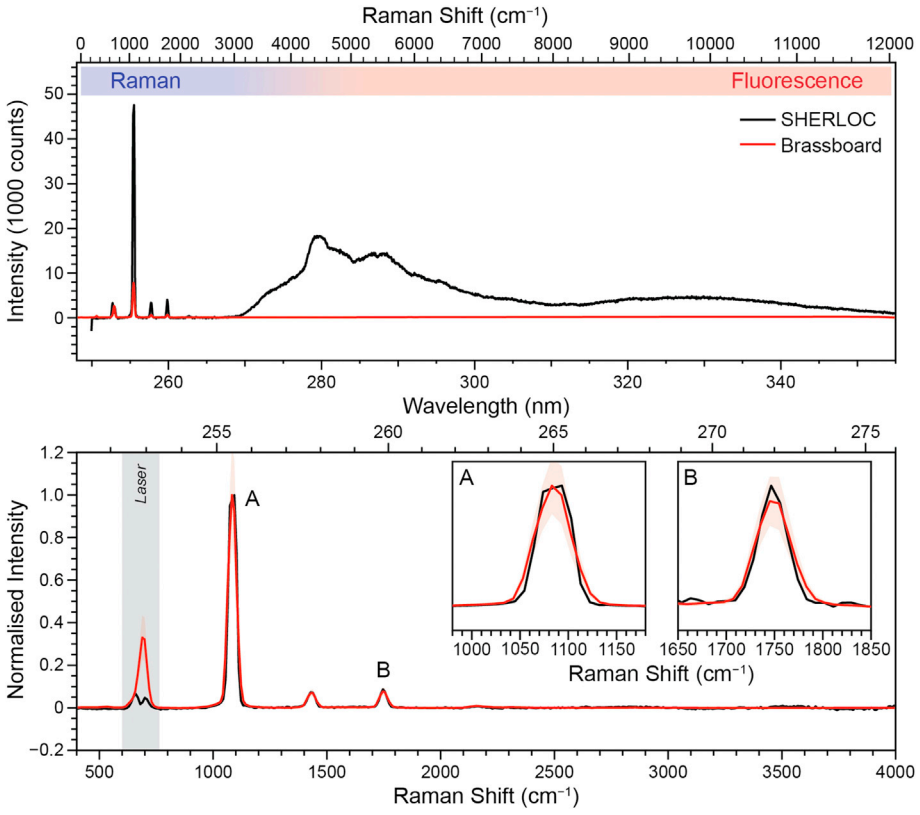

Fig. 2. a) The deep-UV (DUV) spectrum of single-crystal calcite (calcium carbonate), measured using SHERLOC (under simulated Mars ambient conditions) and the Brassboard (under Earth ambient conditions), recorded using 50 and 100 laser pulses per point respectively. b) The normalized Raman region (251–275 nm) of the same spectra after baseline subtraction. Insets: the calcite peaks at ~1085 cm^{-1} (A) and ~1750 cm^{-1} (B). Colored areas indicate ±1 standard deviation of intensity. The vertical grey bar indicates a known NeCu laser emission line at 253.93 nm.

parameters (summarized in Table 2). The more powerful SHERLOC laser produces significantly more Raman scattering with half as many laser pulses (Fig. 2a), but relative intensities between peaks are the same on both instruments (Fig. 2b), and peak shapes are similar (insets). The Brassboard peaks do appear to be slightly wider, consistent with poorer spectral resolution. The appearance of broad fluorescence features in the SHERLOC data is believed to be the result of organic contamination of that sample during testing, rather than innate fluorescence from the calcite mineral itself.

During surface operations, SHERLOC activities will typically consist of 1) Survey/Recon Scans that rapidly cover a large area using fewer laser pulses per point, mainly detecting high-yield fluorescence signals, and 2) Detail Scans that focus on a smaller area of interest with more laser pulses per point to maximize signal from lower-yield Raman scattering. The parameters of each SHERLOC scan can be tailored to the target to ensure the best possible dynamic range for a given operating window, with nominal values of 4–10 pulses per point for a survey scan (approximately 36–90 μJ of total incident laser energy) and 200–900 pulses per point for a Detail Scan (1800–8100 μJ). To replicate these operating regimes with the Brassboard instrument, each mineral sample was scanned multiple times at different laser settings between 5 and 800 pulses per point, with either 15 or 20 A of driving current, to cover a range of laser energies from ~20 to ~4000 μJ.

Fig. 3 shows how the DUV Raman spectrum measured by the Brassboard for single-crystal calcite varied with the total laser energy used, after baseline subtraction and normalization. The calcite peaks at 1085, 1432, and 1754 cm^{-1} do not vary appreciably in position, shape, or their relative intensity, until the dominant peak becomes saturated and flattened at exposures greater than 400 pulses (>1800 μJ). Below 400 pulses, the calcite spectrum varies only in terms of SNR, which is roughly proportional to input energy, and all three peaks are easily detected and identified with only 5 laser pulses (~22 μJ). Such a strong signal most likely results from a large Raman scattering cross-section and because the calcite crystal is relatively transparent to UV, which maximizes the sample volume being probed [Carrier et al., 2019; Razzell Hollis et al., 2020]. This is very encouraging, as it suggests that calcite (and other minerals with similar Raman cross-sections and UV transparencies) will be easily detected by SHERLOC even during routine short-exposure survey scans. Similar figures for all samples in this study may be found in Figs. S11–S16.

We also observed some variation in spectral features that could not be associated with the calcite sample. The intensity of the ~695 cm^{-1} (252.93 nm) laser emission line was much greater when the laser was driven at 20 A compared to 15 A, and was saturated even at 5 pulses per point. A small symmetric peak at ~3350 cm^{-1} was visible in all 20 A spectra as well, and is attributed to specular reflection of a very minor laser emission line at 271 nm. A broad asymmetric feature at ~1200 cm^{-1} was visible for 20 A spectra at 100+ pulses per point, and is likely another laser reflection artifact. Neither the 3350 or 1200 cm^{-1} artifacts were visible in equivalent SHERLOC spectra of single-crystal calcite (see Fig. 2b), due to more effective rejection of secondary laser emission lines by SHERLOC's laser optics. As these artifacts do not appear in Brassboard spectra acquired with only 15 A of current, which also reduces the impact of the 252.93 nm laser line outside the 600–750 cm^{-1} region, we conclude that 15 A Brassboard spectra are closest to what would be observed with SHERLOC. As such, Fig. 4 onwards depict only the best possible sample spectra as measured at 15 A, using either 800 pulses per point or the highest value that did not result in signal saturation (total energies falling between 1800 and 2500 μJ).

3.2. Differentiating mineral classes

Both DUV Raman and Fluorescence spectra were measured for all mineral samples in this study. We found that the majority of samples exhibited little to no DUV fluorescence, and that fluorescence was highly variable, even between samples of the same mineral (see Figs. S6–S10).

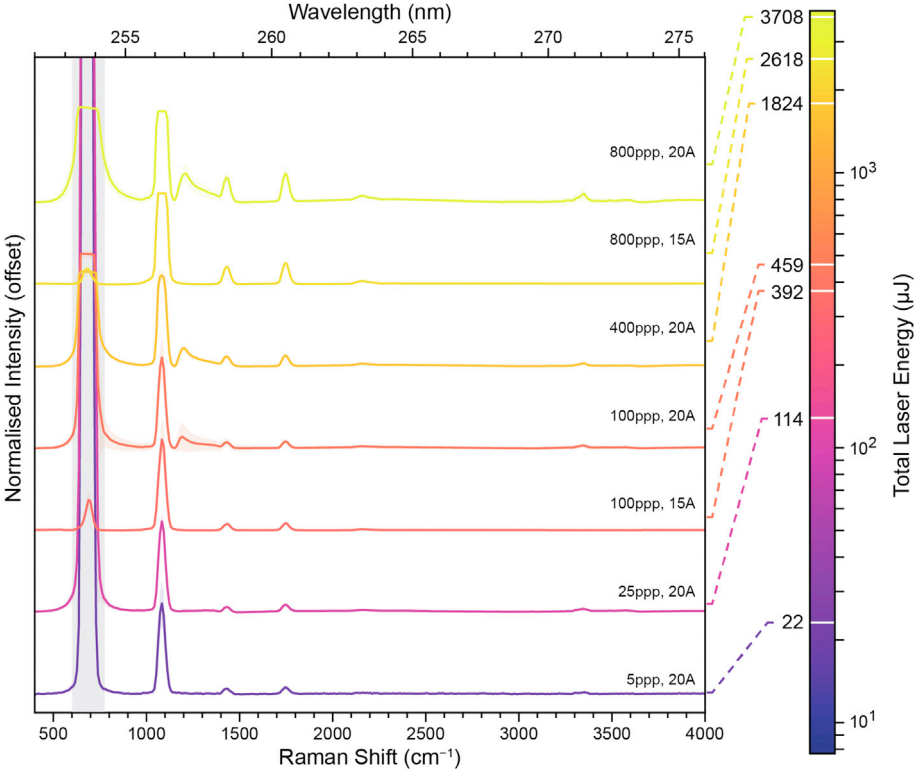

Fig. 3. The DUV Raman spectrum of single-crystal calcite under Earth ambient conditions, measured using different laser settings to explore a range of total exposure energies comparable to different SHERLOC activities. Each spectrum is the average of 25 points, normalized to the peak intensity at ~1085 cm^{-1} after baseline subtraction. Colored areas indicate ±1 standard deviation. The vertical grey bar indicates the region obscured by the NeCu laser emission line at 253.93 nm.

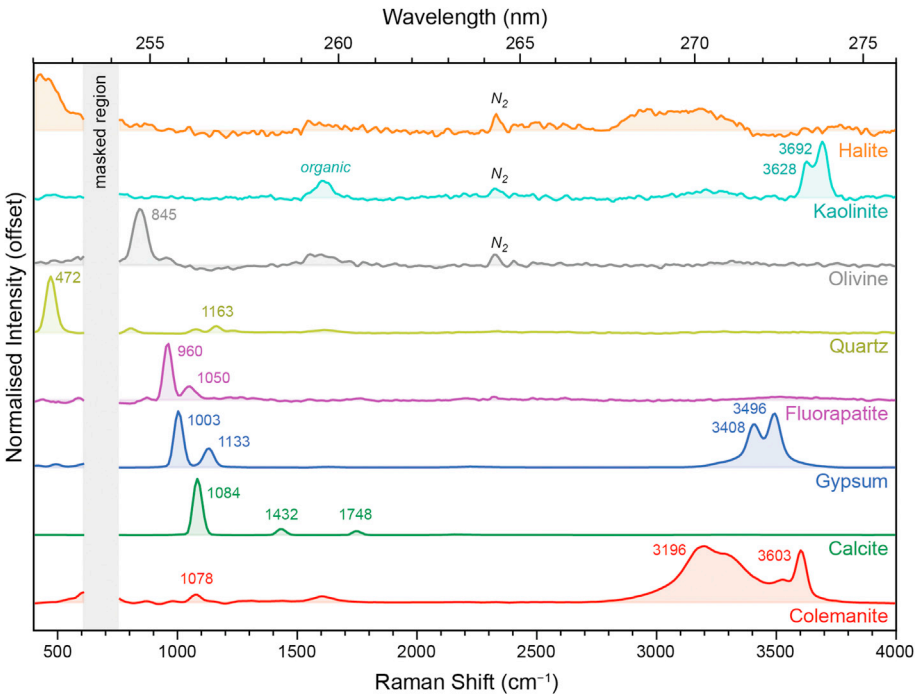

Fig. 4. The Raman region (250–275 nm) of the DUV spectrum for eight minerals of different classes, measured under Earth ambient conditions. Spectra were averaged over 25 points at 800 laser pulses per point (~1800–2600 μJ) under Earth ambient conditions. Spectra were normalized to the maximum intensity in the 400–4000 cm^{-1} region after baseline subtraction. The vertical grey bar indicates a region obscured by laser emission; numbers indicate the average position (in cm^{-1}) of key peaks.

We concluded that fluorescence was not a reliable identifier of mineral composition, as we could not confirm that it was innate to the mineral and not the result of trace quantities of rare earth elements and/or organic material present within the mineral matrix [Eshelman et al., 2019; Martin et al., 2020; Shkolyar et al., 2018 & 2021]. As such, we have instead focused on Raman spectra for identifying minerals in this paper.

Fig. 4 shows the DUV Raman spectra obtained for eight minerals that exemplify different classes of mineral potentially relevant to the geological history of Jezero crater. They include colemanite (calcium triborate hydrate), calcite (calcium carbonate), gypsum (calcium sulfate dihydrate), fluorapatite (calcium fluorophosphate), olivine (an orthosilicate), quartz (a tectosilicate), kaolinite (a phyllosilicate), and halite (sodium chloride). With the exception of halite, all of these minerals produced detectable Raman scattering, exhibiting a number of relatively narrow peaks between 400 and 1800 cm^{-1} that are assigned to the *internal vibrational modes* of the covalently-bonded [BO_3]/[BO_4], [CO_3], [SO_4], [PO_4], or [SiO_4] units of each mineral [Griffith, 1969]. The presence of hydrated/hydrous minerals may also be detected by one or more strong, very broad peaks between 3000 and 3600 cm^{-1} produced by scattering from the internal vibrations of H_2O, exemplified in Fig. 4 by colemanite and gypsum, while sharp narrow peaks around 3600–3700 cm^{-1} tend to be stretching modes of OH (hydroxyl) groups, as exemplified by kaolinite. As low-frequency *lattice modes* are outside SHERLOC's wavelength range, minerals such as halite that lack covalent bonds are not expected to produce detectable Raman scattering. The spectra of low-signal or Raman-inactive samples (such as halite) are instead dominated by background noise and the very weak, narrow Raman peaks of terrestrial atmospheric N_2 and O_2 at ~2330 and ~1550 cm^{-1} respectively, which will not be observed in SHERLOC spectra taken on Mars due to their significantly lower partial pressures in the Martian atmosphere.

The specificity of vibrational modes to chemical structure means the pattern of Raman peaks and their positions, tabulated for all samples in Table 4, can be used to easily distinguish different classes of mineral as long as their Raman scattering can be detected. The relatively simple stoichiometry and symmetry of the carbonate, sulfate, and phosphate units means they only have a few Raman-active vibrational modes, typically referred to as ν_1 (a symmetric stretching mode), ν_2 (out-of-plane bending), ν_3 (anti-symmetric stretching), and ν_4 (in-plane bending) [Griffith, 1969]. For the carbonate, sulfate, and phosphate minerals in Fig. 4, the ν_1 vibration is the strongest peak in the spectrum and its general position is the first indication of a mineral's classification, occurring at ~1100 cm^{-1} in carbonates, ~1000 cm^{-1} in sulfates, and ~950 cm^{-1} in phosphates. Each class exhibited two or three minor modes at other frequencies that can aid classification: carbonate minerals typically have a ν_3 mode at ~1440 cm^{-1} and a combined $\nu_1 + \nu_4$ mode at ~1750 cm^{-1}, sulfate minerals have a ν_2 mode at ~500 cm^{-1} and a ν_3 mode at ~1130 cm^{-1}, while phosphate minerals have a ν_3 mode at ~1050 cm^{-1}.

Borate minerals tend to have many vibrational modes between 900 and 1800 cm^{-1} due to the more complex symmetry of the polymeric borate ion, which is made up of covalently bonded boron units with trigonal and tetrahedral coordination, referred to as [BO_3] and [BO_4]. Colemanite exhibited a strong symmetric stretching mode around 900–1100 cm^{-1}, which risks confusion with the characteristic peak positions associated with carbonate, sulfate, and phosphate minerals, but can still be easily distinguished by the number and pattern of minor modes between 900 and 1800 cm^{-1}, and the presence of a sharp, strong B–OH hydroxyl stretching mode at ~3580 cm^{-1}.

The silicate minerals tend to have relatively simple spectra with few peaks, but show significant variation in the number and position of the peaks due to the markedly different structures adopted by the silicate lattice, exemplified in Fig. 4 by quartz, olivine, and kaolinite. The dominant peak we observed for quartz (a tectosilicate) was a Si–O–Si bending mode at ~475 cm^{-1}, for olivine (an orthosilicate) it was a Si–O stretching mode at ~845 cm^{-1}, and for kaolinite (a phyllosilicate) it was a pair of Si–OH hydroxyl stretching modes at ~3630 and ~3690 cm^{-1}.

In addition to mineralogy, DUV Raman can also provide information on the presence of organic material within the mineral matrix or on its surface. Strong UV absorption by aromatic organic compounds can lead to intense fluorescence, as well as fulfilling the conditions for resonant Raman, which results in significantly higher Raman scattering yields compared to Raman from non-resonant compounds [Abbey et al., 2017; Bhartia et al., 2021]. The presence of organic contaminants in a natural mineral sample is typically observable by the appearance of a broad

Table 4
DUV Raman peak positions (in cm^{-1}) obtained by fitting the major peaks for each mineral sample, and their assignments to specific internal vibrational modes. All reported positions have a combined uncertainty of ±5 cm^{-1} from calibration and fitting, and *n.d.* indicates the peak was not detectable. Sample references are given as follows:[1] Razzell Hollis et al. (2021a);[2] Thomas et al. (2018);[3] McCollom et al. (2014);[4] Ehlmann (2010);[5] Fox et al. (2021);[6] Buz and Ehlmann (2017). * indicates a synthetic mineral. Key to assignments: ν_i = internal vibration *i*; *S.* = stretching mode; *B.* = bending mode; *G.* = graphitic carbon band; *D.* = defective carbon band. *n.d.* indicates the peak was not detected, blank spaces indicate the peak was not expected to be present.

Mineral	Sample					
Borates		$[BO_3]/[BO_4]$ (*S.*)	B–OH (*B.*)	B–OH (*S.*)	H_2O (*S.*)	Organic (*G.*)
Colemanite	Powder[1]	1079	*n.d.*	3606	3215	
Kernite	Crystal[1]	931	1333	3553	3324	
Ulexite	Crystal[1]	985	1372	3576	3416	
Carbonates		$[CO_3]$ ν_1 (*S.*)		$[CO_3]$ ν_3 (*S.*)	$[CO_3]$ $\nu_1 + \nu_4$ (*S.*+*B.*)	Organic (*G.*)
Aragonite	Crystal	1091		1465	1748	
Calcite	Crystal[1]	1085		1432	1745	
	Powder[1]	1085		1434	1749	
	Pellet[2]	1091		1439	1754	
Chalk	Rock[1]	1089		1433	1752	1610
Dolomite	Crystal[1]	1099		1444	1761	
	Powder[1]	1097		1443	1760	
	Pellet[2]	1102		1441	1764	1615
Magnesite	Crystal[1]	1099		1452	1768	
	Powder[1]	1094		1446	1762	
Nahcolite	Powder[1,*]	1044		1441	1678	
	Pellet	1051		1448	1683	
Rhodochrosite	Crystal[1]	1091		1423	1733	
	Powder[1]	1084		1416	1726	
Siderite	Crystal[1]	*n.d.*		*n.d.*	*n.d.*	
Trona	Powder[1,*]	1061		1427	1715	
Phosphates		$[PO_4]$ ν_1 (*S.*)		$[PO_4]$ ν_3 (*S.*)		Organic (*G.*)
Fluorapatite	Crystal	960		1050		
Sulfates		$[SO_4]$ ν_1 (*S.*)	$[SO_4]$ ν_2 (*B.*)	$[SO_4]$ ν_3 (*S.*)	H_2O (*S.*)	Organic (*G.*)
Anhydrite	Powder[1]	1014	494	1128	3408, 3496	
Barite	Powder[1,*]	984	458	1138		
Epsomite	Powder[1,*]	983, 1036	*n.d.*	1112	3410	
Gypsum	Crystal[1]	1009	494	1134	3411, 3500	
	Powder[1]	1004	494	1131	3408, 3497	
	Pellet[2]	1014	504	1138	3415, 3503	
Kieserite	Powder*	979, 1033	459	1115	3414	
Melanterite	Powder[1]	1014	*n.d.*	1191	3234	
Natroalunite	Pellet 6[3,*]	1021	494	1163	3468	
Natroalunite-Natrojarosite	Pellet 1[3,*]	*n.d.*	*n.d.*	*n.d.*		
	Pellet 10[3,*]	*n.d.*	*n.d.*	*n.d.*		
Natrojarosite	Pellet 9[3,*]	*n.d.*	*n.d.*	*n.d.*		
	Powder[1]	*n.d.*	*n.d.*	*n.d.*		
Thenardite	Powder[1]	991	*n.d.*	1126		
Fe^{III} Sulfate	Pellet[2,*]	*n.d.*	*n.d.*	*n.d.*		
Fe^{II} Sulfate	Pellet*	987	*n.d.*	1123	3418	
	Powder[1]	986	*n.d.*	1123	3424	
Mg Sulfate	Pellet[2,*]	992	471	1157	3428	
	Pellet*	1020	484	1150	3440	
Na Sulfate	Pellet[2,*]	998	468	1135		
	Pellet*	998	468	1135		
Halides		H_2O (*B.*)	H_2O (*S.*)	$[NH_4]$ ν_1 (*S.*)	$[NH_4]$ ν_2 (*B.*)	Organic (*G.*)
Halite	Crystal[1]					
	Pellet[2]					1615
K Bromide	Pellet*					
Mg Chloride	Pellet*	1589	3363, 3500			
Ca Chloride	Pellet*	1638	3448			
Ammonium Chloride	Pellet*			3051	1716	
Oxides and Hydroxides		MO_X (*S.*)	MO_X (*B.*)	M–OH (*S.*)		Organic (*G.*)
Hematite	Powder*	*n.d.*	*n.d.*			
Manganite	Rock	*n.d.*	465			1569
Brucite	Pellet[2]			3653		
Silicates (by type)		$[SiO_4]$ ν_1 (*S.*)	$[SiO_4]$ ν_4 (*B.*)	Si–OH (*S.*)		Organic (*G.*)
Silica phases						
Quartz	Powder[1]	1079, 1162, 1232	474			
	Pellet[2]	1090, 1168, *n.d.*	477			1600
Opal	Crystal	*n.d.*	435			1608
	Pellet[2]	1078	485			1618
Glasses						
Basaltic Glass	Pellet[4]	*n.d.*	*n.d.*			
Pyroxenes						
Augite	Powder	1014	*n.d.*			
	Pellet	1000	*n.d.*			

(*continued on next page*)

Table 4 (*continued*)

Mineral	Sample					
Diopside	Crystal	1017	*n.d.*			
	Pellet	1014	*n.d.*			
Enstatite	Crystal	1026	*n.d.*			
	Powder	1021	*n.d.*			
	Pellet	1014	*n.d.*			
Hedenbergite	Crystal	*n.d.*	*n.d.*			
	Pellet	*n.d.*	*n.d.*			
Plagioclases						
Albite	Crystal	*n.d.*	*n.d.*			
Bytownite	Pellet	1014	*n.d.*			1598
Labradorite	Powder	1003	*n.d.*			
Olivines						
Fayalite	Crystal	*n.d.*	*n.d.*			
Forsterite	Crystal	844	*n.d.*			
Olivine	Pellet 1[6]	846	*n.d.*			
	Pellet 2[6]	847	*n.d.*			
	Pellet 3[6]	847	*n.d.*			
	Pellet 4[6]	*n.d.*	*n.d.*			
K-Feldspars						
Microcline	Crystal	1114	504			
Orthoclase	Crystal	1113	494			
Other Silicates						
Epidote	Pellet[2]	*n.d.*	*n.d.*			
Topaz	Pellet[2]	929	*n.d.*	3652		1611
Phyllosilicates		[SiO_4] ν_1 (*S.*)		Si–OH (*S.*)		Organic (*G.*)
Clays						
Chlorite	Pellet	*n.d.*				1578
Illite	Pellet	*n.d.*		*n.d.*		
Kaolinite	Powder	*n.d.*		3632, 3696		1609
Montmorillonite	Powder	*n.d.*		*n.d.*		1592
Smectite	Powder A[5,*]	*n.d.*		*n.d.*		
	Powder G[5,*]	*n.d.*		*n.d.*		
	Powder H[5,*]	*n.d.*		*n.d.*		
	Powder J[5,*]	*n.d.*		*n.d.*		
	Powder K[5,*]	*n.d.*		*n.d.*		
	Powder N[5,*]	*n.d.*		*n.d.*		
Micas						
Biotite	Crystal	*n.d.*				
Muscovite	Crystal	*n.d.*		3627		
	Pellet[2]	*n.d.*		3636		1584
Serpentines						
Antigorite	Pellet	*n.d.*		3679		
Serpentine	Pellet[2]	1054		3691		1605
Serpentinite	Rock	*n.d.*		3680		1600

Raman peak around ~1600 cm^{-1}, such as is seen for kaolinite and possibly olivine in Fig. 4, and sometimes accompanied by a second, weaker peak at ~1400 cm^{-1}. These peaks are typically not specific to a particular organic compound but are more like a weighted average of the continuum of vibrational modes for all organic molecules present, similar to the graphitic 'G' and defective 'D' bands reported for kerogenous organic material on Earth and for refractory organic material detected in Martian meteorites [Schopf et al., 2005; Steele et al., 2016; Shkolyar et al., 2018]. We found similar evidence of organic contamination in several samples (mainly the pelleted samples) but cannot determine if the organics were present in the original rock or introduced later during handling. We note that the pellets from Thomas et al. (2018) were originally made for calibrating the ChemCam instrument, which was not designed to detect organics, and as such contamination may not have been a concern during preparation. Given the sensitivity of SHERLOC to organics, especially aromatics, it's possible that organic concentrations in these samples could be as low as <1 ppm and still be detectable [Abbey et al., 2017], but further analysis of the organics in these samples is beyond the scope of this paper and warrants a separate, more detailed study.

3.3. Differentiating similar minerals

Borates. Three borate minerals were measured: colemanite (calcium borate hydrate), kernite (sodium borate hydrate) and ulexite (sodium calcium borate hydrate). Fig. 5 shows that the borate samples exhibited significant variance in the pattern of their DUV Raman peaks between 800 and 1800 cm^{-1}, and around 3300 cm^{-1}, as we have reported previously [Razzell Hollis et al., 2021a]. The large variation in spectra corresponds to significant differences in vibrational modes resulting from different internal structures of the polymeric borate unit, which forms triborate $[B_3O_4(OH)_3]^{2-}$ in colemanite, pentaborate $[B_5O_6(OH)_6]^{3-}$ in kernite, and tetraborate $[B_4O_6(OH)_2]^{2-}$ in ulexite [Kloprogge and Frost, 1999; Frost et al., 2013]. The dominant peak in the 800–1800 cm^{-1} region occurred at 1079 cm^{-1}, in colemanite, 931 cm^{-1} in kernite, and 985 cm^{-1} in ulexite, and was assigned to the symmetric stretching mode of either trigonally coordinated [BO_3] (around ~950 cm^{-1}) or tetrahedrally coordinated [BO_4] (around ~1080 cm^{-1}). The bending mode of B–OH appears as a broad, asymmetric peak around ~1350 cm^{-1}, while the stretching mode of the B–OH hydroxyl was a relatively narrow, very strong peak at ~3580 cm^{-1}. Peak assignments were made based on previous DUV measurements and reported vibrational frequencies in the literature [Kloprogge and Frost, 1999; Razzell Hollis et al., 2021a]. The hydration of all three minerals was evident in the appearance of a strong, broad peak around 3000–3600 cm^{-1}.

Regarding SHERLOC's ability to detect and identify borate minerals by their DUV Raman spectra, the most readily distinguished feature was the B–OH hydroxyl stretching mode at ~3580 cm^{-1}, which was 5–10x stronger than the trigonal/tetrahedral stretching modes at 900–1100 cm^{-1} and could still be detected with only 5 laser pulses

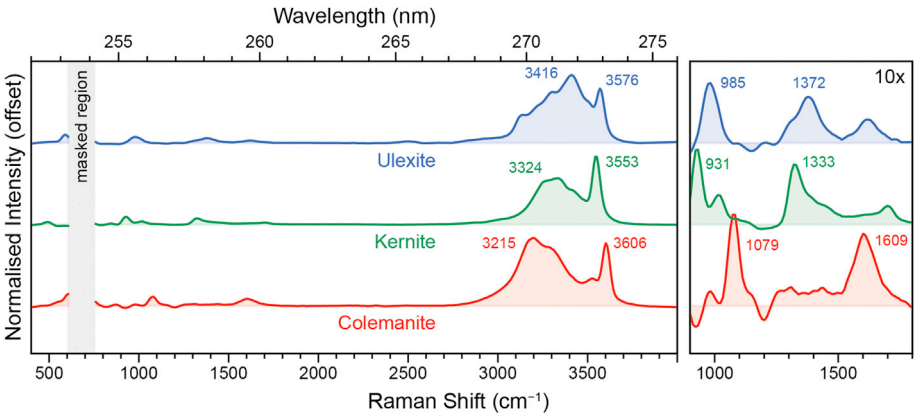

Fig. 5. DUV Raman spectra for various borate mineral samples, measured under Earth ambient conditions. See Fig. 4 for a summary of acquisition parameters and spectral processing.

(~19 μJ). Furthermore, its position was highly characteristic of the specific mineral in question, occurring at 3606 cm^{-1} in colemanite, 3553 cm^{-1} in kernite, and 3576 cm^{-1} in ulexite. With a total spread of 53 cm^{-1}, it should be easy to identify different borate minerals from their SHERLOC spectra, even in low SNR samples where the internal vibrations at 800–1800 cm^{-1} cannot be detected.

Carbonates. Eight different carbonate minerals were measured: aragonite (orthorhombic calcium carbonate), calcite (trigonal calcium carbonate), chalk (biogenic calcium carbonate rock), dolomite (calcium magnesium carbonate), magnesite (magnesium carbonate), rhodochrosite (manganese carbonate) and siderite (iron carbonate), as well as two bicarbonate-bearing minerals, nahcolite (sodium bicarbonate), and trona (sodium sesquicarbonate hydrate). As shown in Fig. 6, the majority of carbonate samples exhibited well-defined Raman spectra that were dominated by the $[CO_3]$ ν_1 peak at 1080–1100 cm^{-1}, along with the minor ν_3 and $\nu_1 + \nu_4$ peaks at ~1440 and ~1750 cm^{-1}. Assignments were made based on previous measurements and reported vibrational frequencies in the literature [Griffith, 1969; Razzell Hollis et al., 2021a], however, there is not a consensus regarding assignment of the ~1750 cm^{-1} peak to the $\nu_1 + \nu_4$ mode, which is sometimes assigned to the overtone $2\nu_2$ [Bischoff et al., 1985].

The carbonate minerals tended to produce very strong Raman spectra and the majority produced clearly detectable Raman spectra even with only 5 laser pulses per point (~20 μJ). The exception was siderite, which only exhibited peaks attributable to atmospheric O_2 and N_2, with no carbonate peaks observable even at a long exposure of 3000 μJ. We attribute this lack of signal to the presence of Fe in siderite, as $Fe^{2+/3+}$ ions are known to have strong absorption coefficients in the UV, which will limit the penetration of the DUV laser into the sample as well as attenuating any outbound Raman scattering [Shkolyar et al., 2018; Carrier et al., 2019].

Perhaps the most significant spectral variation between different carbonate minerals was the average position of the dominant ν_1 mode, which was found between 1084 and 1102 cm^{-1} for the purely $[CO_3]$-

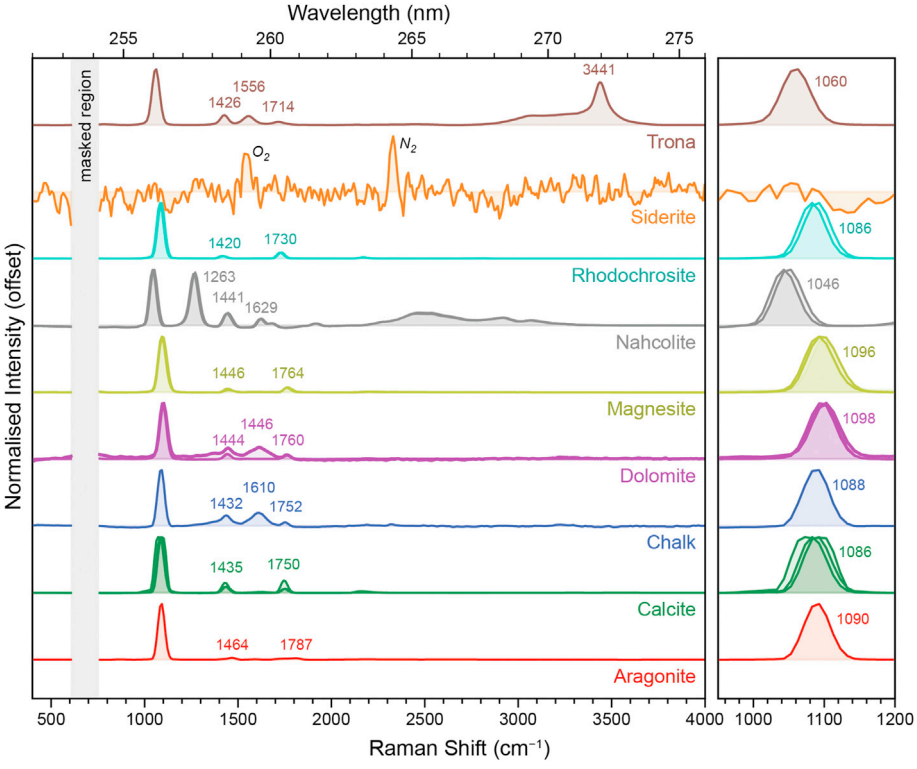

Fig. 6. DUV Raman spectra for various carbonate mineral samples, measured under Earth ambient conditions. See Fig. 4 for a summary of acquisition parameters and spectral processing.

bearing minerals and at significantly lower frequencies for those minerals containing the bicarbonate ion [HCO_3], with nahcolite appearing at 1044–1051 cm^{-1}, and trona appearing at 1061 cm^{-1}. The significant change in ν_1 position between nahcolite, trona, and the other carbonates can be understood as the change in electronic structure and bond strength between bicarbonate [HCO_3] and carbonate [CO_3] ions, which leads to an appreciable change in vibrational frequencies for the oxyanion.

The range of observed ν_1 positions (average position in brackets) for each [CO_3]-bearing mineral was as follows: aragonite: 1091 cm^{-1}; calcite: 1085–1091 cm^{-1} (1087 cm^{-1}); chalk: 1089 cm^{-1}, dolomite: 1097–1102 cm^{-1} (1099 cm^{-1}); magnesite: 1094–1099 cm^{-1} (1096 cm^{-1}); and rhodochrosite: 1084–1091 cm^{-1} (1087 cm^{-1}). The variation originates in the different electrostatic environment experienced by the carbonate oxyanion in each mineral, a consequence of any differences in either lattice structure or the radius and/or charge of the metallic cation. These factors act to perturb the covalent bonds of the oxyanion and alter their frequency of vibration, a phenomenon that has also been reported for visible Raman and infrared absorption of carbonate minerals and is expected to apply to sulfate and phosphate minerals as well [Adler and Kerr, 1963; Kaabar et al., 2011; Chan et al., 2017]. Previous DUV Raman studies on carbonates suggest that some of the observed variation in peak position between samples of the same mineral may reflect minor differences in elemental composition [Razzell Hollis et al., 2021a].

With the exception of siderite, all the carbonate minerals had at least two minor peaks at ~1440 and ~1750 cm^{-1}. The positions of these peaks also varied from mineral to mineral, the ν_3 mode varying by ~49 cm^{-1} between 1416 and 1465 cm^{-1}, and the $\nu_1 + \nu_4$ mode varying by ~90 cm^{-1} between 1678 and 1768 cm^{-1}. As we have reported previously, the position of the ~1750 cm^{-1} peak appears to be positively correlated with the position of the ν_1 at ~1080 cm^{-1} (see Fig. S17), which supports assignment to a combined $\nu_1 + \nu_4$ mode [Razzell Hollis et al., 2021a].

Additional peaks were observed for certain samples, including nahcolite, trona and limestone chalk. Nahcolite and trona exhibited additional peaks resulting from the altered symmetry of the [HCO_3] bicarbonate ion, appearing in nahcolite as a second strong peak at 1264–1270 cm^{-1} and an extra minor peak at 1620–1626 cm^{-1}, while trona had an additional minor peak at 1557 cm^{-1} [Razzell Hollis et al., 2021a]. Trona was the only carbonate mineral to show any evidence of hydration, appearing as a strong bimodal peak with a maximum at 3444 cm^{-1}. The presence of organic material was also observed in two samples by the appearance of an additional minor peak around 1610 cm^{-1} for the limestone chalk sample and around 1615 cm^{-1} in the dolomite mix7-O pellet sample. In both cases the peak position and shape was consistent with the G band of kerogenous organic material, consistent with both samples being comprised of natural mineral that may have entrapped organics that then degraded over time, becoming kerogenous.

The position of the ν_1 peak appears to be the most characteristic parameter for identifying different carbonate minerals, however in certain cases the difference in peak position between two distinct minerals is smaller than the sample-to-sample variation for a particular mineral (2–8 cm^{-1}) or the estimated uncertainty of measured peak positions (±5 cm^{-1}). The uncertainty also accounts for the discrepancy between these observations and reported literature values for the same minerals, e.g. 1087 cm^{-1} for calcite's ν_1 peak [De La Pierre et al., 2014]. Identification may be improved by considering the positions of the minor peaks, for example: aragonite and calcite have both been observed with ν_1 positions of ~1090 cm^{-1}, but can be distinguished by the position of the ν_3 mode at 1465 cm^{-1} in aragonite and 1432–1439 cm^{-1} in calcite. Given the exceptional Raman signal we observe for carbonate minerals (with the exception of siderite), which means the ν_3 and $\nu_1 + \nu_4$ modes are easily detected even at short exposures, identification of specific carbonate minerals should be possible on Mars.

Sulfates. Fourteen sulfate-bearing samples were measured, including the minerals anhydrite (calcium sulfate), barite (barium sulfate), epsomite (sodium sulfate heptahydrate), gypsum (calcium sulfate dihydrate), kieserite (magnesium sulfate hydrate), melanterite (iron sulfate heptahydrate), natroalunite (sodium aluminum sulfate hydroxide), natrojarosite (sodium iron sulfate hydroxide), and thenardite (sodium sulfate), as well as two unnamed minerals in the Al–Fe solid solution series between natroalunite and natrojarosite with relative Fe contents of 61% and 92%, and four synthetic salts of magnesium sulfate, iron(II) sulfate ($FeSO_4$), iron(III) sulfate ($Fe_2(SO_4)_3$), and sodium sulfate.

The sulfate minerals consistently produced DUV Raman spectra dominated by the [SO_4] ν_1 mode at ~1000 cm^{-1}, with the [SO_4] ν_2 and ν_3 modes appearing as minor peaks at ~470 and ~1150 cm^{-1} (see Fig. 7). Assignments were made based on previous measurements and reported vibrational frequencies in the literature [Griffith, 1969; Brotton and Kaiser, 2013; Mabrouk et al., 2013; Razzell Hollis et al., 2021a]. Of the sulfate minerals we examined, four samples did not provide a detectable DUV Raman spectrum at laser exposures up to ~3000 μJ: the Fe-bearing mineral natrojarosite, the two natroalunite-natrojarosite synthetic mixtures (which had relative Fe site occupancies of 61% and 92% by mole), and the iron(III) sulfate, $Fe_2(SO_4)_3$. We consider the lack of signal from these samples to be further confirmation that Fe-rich minerals can reduce DUV Raman signal to undetectable levels. However, Fe content cannot be the only factor that determines detectability as the Raman peaks of [SO_4] could still be detected for relatively Fe-rich samples of melanterite ($FeSO_4 \cdot 7H_2O$) and iron(II) sulfate ($FeSO_4$). As the opto-electronic properties of Fe ions within the mineral will depend on a combination of their ionic charge and coordination [Rossman and Ehlmann, 2019], it is not unreasonable to see significant variations in overall UV absorption (and therefore measured Raman signal) between different minerals of similar Fe content.

Fig. 7 shows how the measured DUV Raman spectrum varied between different sulfate minerals, and between samples of the same mineral. Like the carbonates, the most significant distinction between individual sulfate minerals is the position of the ν_1 peak, which varied by ~57 cm^{-1} between 979 and 1036 cm^{-1}. The range of observed ν_1 positions (and the average, where applicable) for each of the sulfate minerals was as follows: anhydrite: 1014 cm^{-1}; barite: 984 cm^{-1}; epsomite: 983 cm^{-1}; gypsum: 1004–1014 cm^{-1} (1009 cm^{-1}); kieserite: 979 cm^{-1}; melanterite: 1014 cm^{-1}; natroalunite: 1021 cm^{-1}; and thenardite: 991 cm^{-1}. For the synthetic sulfates the ν_1 peak was observed at 987 cm^{-1} in iron(II) sulfate, 992–1020 cm^{-1} (1006 cm^{-1}) in magnesium sulfate, and 998 cm^{-1} in sodium sulfate. The ν_1 peak was more difficult to assign for kieserite ($MgSO_4 \cdot H_2O$) and epsomite ($MgSO_4 \cdot 7H_2O$) as both exhibited two ν_1 peaks at ~980 and ~1035 cm^{-1}, with the 980 cm^{-1} peak dominating in kieserite and the 1035 cm^{-1} peak dominating in epsomite. This is unexpected as visible wavelength Raman studies of $MgSO_4$ hydrates have previously reported the ν_1 mode of pure epsomite to occur at ~985 cm^{-1}, shifting to ~1045 cm^{-1} for pure kieserite, which suggests that the hydration of these samples may have changed in the time since they were identified [Wang et al., 2006]. We note that the two different sample pellets of synthetic $MgSO_4$ exhibited singular peaks at two different positions, 992 cm^{-1} and 1020 cm^{-1} respectively, suggesting that these samples exhibiting two distinct hydration states intermediate between kieserite and epsomite [Wang et al., 2006].

The minor ν_2 and ν_3 modes at ~450 and ~1150 cm^{-1} also showed variation in their positions between different sulfate minerals, between 46 and 79 cm^{-1} respectively. There appears to be some positive correlation between the positions of the anti-symmetric ν_3 and symmetric ν_1 stretching modes, with a higher Raman shift for ν_3 tending to coincide with a higher shift for ν_1 (see Fig. S18). However, identification of the ν_3 position can be muddled by the presence of additional strong or overlapping peaks in the 1000–1200 cm^{-1} region for some minerals, including epsomite, kieserite, and melanterite, and requires careful deconvolution to determine the correct peak positions.

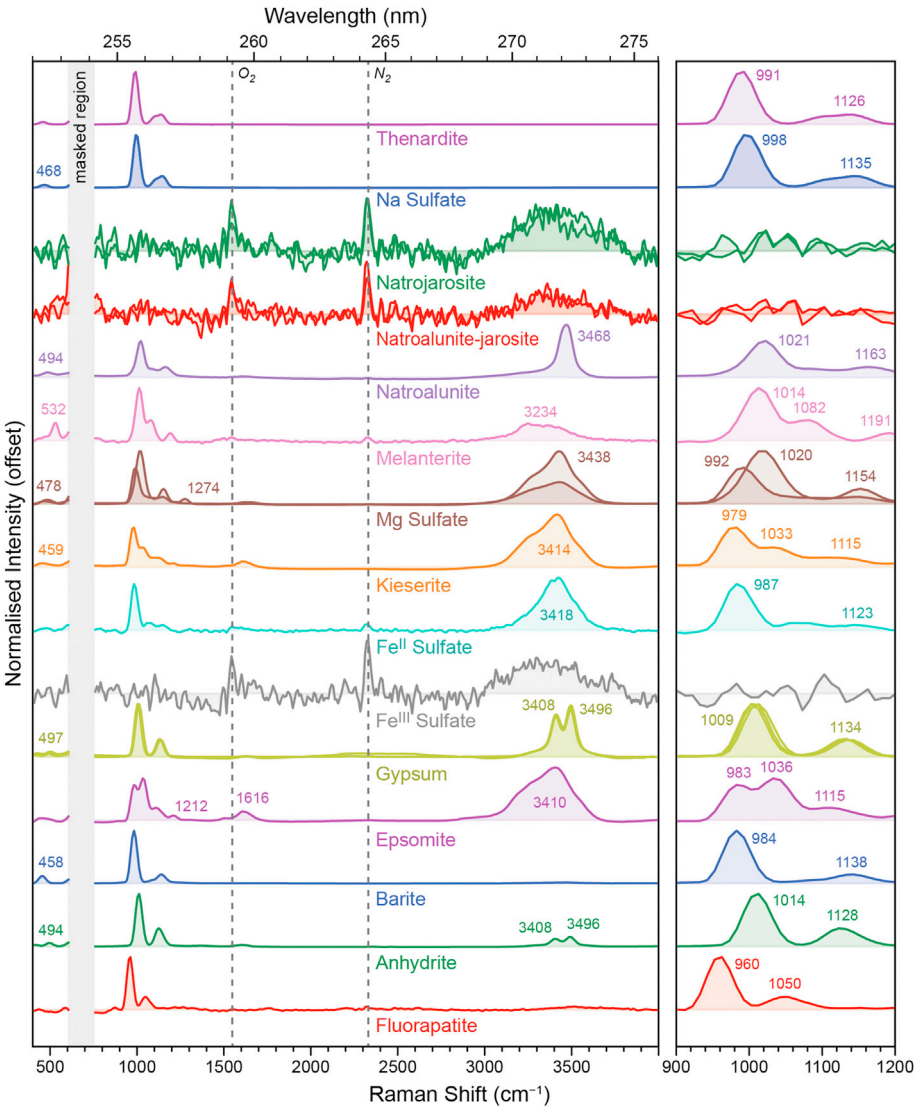

Fig. 7. DUV Raman spectra for various sulfate mineral samples and a single phosphate mineral, fluorapatite, as measured under Earth ambient conditions. See Fig. 4 for a summary of acquisition parameters and spectral processing.

Many of the sulfate minerals had one or more broad Raman peaks around 3300 cm^{-1}, indicative of hydration. Gypsum and anhydrite both exhibited a doublet of relatively narrow peaks at 3411 and 3500 cm^{-1}, a limited number of well-defined vibrational frequencies being typical of their low hydration state (e.g. dihydrate in gypsum). Although anhydrite is formally defined as anhydrous calcium sulfate, the appearance and positioning of the hydrate doublet is consistent with previous measurements that this particular sample contains ~15% gypsum [Razzell Hollis et al., 2021a]. At the other extreme of hydration were the samples of epsomite, iron(II) sulfate, kieserite, magnesium sulfate, and melanterite, which all exhibited extremely broad bimodal peaks with maxima falling across a wide range, 3230–3500 cm^{-1}, typical of higher hydration states (e.g. epsomite) that produce a broad range of vibrational frequencies for the H_2O stretching mode. Natroalunite exhibited a single narrow peak at 3468 cm^{-1}, which may be the stretching mode of the Al–OH hydroxyl rather than H_2O.

Like the carbonates, it appears that the ν_1 peak is the best parameter for identifying different sulfate minerals from their SHERLOC spectra, based on its detectability and its variation in position between minerals. Variability between samples of the same mineral was similar to that observed for the carbonates, with a range of ~9 cm^{-1} observed across three samples of gypsum. However, because the overall range of frequencies observed is larger than that of the carbonate minerals, the sulfate minerals are easier to distinguish from one another. Identification may be aided by determining the position of the minor ν_3 mode at ~1150 cm^{-1} provided that it can be detected, but, as shown by the natrojarosite samples, detectability may be hampered by strong UV absorption of Fe-rich minerals.

Phosphates. A single phosphate mineral was measured to provide a comparison between phosphate and sulfate DUV Raman spectra. Fluorapatite (calcium fluorophosphate) exhibited a spectrum dominated by the [PO_4] ion's ν_1 mode at 961 cm^{-1} and a single minor ν_3 mode at 1050 cm^{-1} (Fig. 7). Peak assignments were determined by comparison to previous DUV measurements [Abbey et al., 2017] and reported assignments in the literature under visible excitation [Griffith, 1969;Litasov and Pogdornykh, 2017]. The flourapatite spectrum appears very similar to those of the sulfate minerals, indicative of the similar structures and symmetries of the [PO_4] and [SO_4] ions, but is shifted to lower frequencies as a result of a longer average bond length. Indeed, the ν_1 position of fluorapatite was shifted by at least 20 cm^{-1} compared to even the lowest sulfate mineral we investigated, which suggests that SHERLOC will be able to easily differentiate between sulfate and phosphate minerals based on peak positions.

Halides. In addition to the mineral halite (NaCl), we also measured four other halide-bearing salts: calcium chloride ($CaCl_2$), magnesium

chloride ($MgCl_2$), potassium bromide (KBr), and ammonium chloride (NH_4Cl). Like halite, the majority of these samples lack covalent bonds and thus the only innate Raman scattering they should generate are from lattice modes, which occur at very low Raman shifts that fall outside the range we can reliably observe with SHERLOC. However, many samples show evidence of detectable Raman scattering from other components, such as H_2O or organic material (see Fig. 8). The exception was ammonium chloride, as the internal vibrational modes of the ammonium [NH_4] cation produce a strong Raman peak at 3051 cm^{-1} and a minor peak at 1716 cm^{-1}, which are respectively assigned to the ν_1 (symmetric stretching) mode and ν_2 (out-of-plane bending) mode of [NH_4] [Krishnan, 1947]. Fitting also resolved the position of an overlapping peak at ~3120 cm^{-1}, consistent with the ν_3 (anti-symmetric stretching) mode described by Krishnan [1947], as well as a minor peak at 2841 cm^{-1} that was unassigned.

Organic contamination was potentially observed in the synthetic halite "mix14-O″ sample, appearing as a relatively weak broad peak at 1615 cm^{-1}. The peak was very weak, barely double the intensity of the atmospheric N_2 peak at 2333 cm^{-1}, suggesting a fairly low concentration considering the sensitivity of DUV Resonant Raman spectroscopy to such material [Asher et al., 1986; Abbey et al., 2017; Razzell Hollis et al., 2020;Razzell Hollis et al., 2021b].

Of the halide samples we examined, two showed evidence of hydration: calcium chloride exhibited a relatively narrow, strong Raman peak at 3448 cm^{-1}, while magnesium chloride exhibited a doublet of relatively narrow peaks at 3363 and 3500 cm^{-1}. Both features are consistent with the stretching mode of H_2O existing as hydrate in a crystalline lattice, with the relative narrowness and unimodal shape of the peaks indicating a low hydration state with a well-defined vibrational frequency. These are hygroscopic phases, and hydration was likely introduced by absorption of ambient H_2O during pellet preparation or sample storage. The shapes and positions of such peaks are known to be specific to the hydrated salt, and may be a means by which SHERLOC can detect hydrated halide salts despite the lack of detectable Raman scattering from the salt itself.

Metal Oxides and Hydroxides. Three metal oxide/hydroxide minerals were measured: hematite (iron(III) oxide, Fe_2O_3), manganite (manganese oxide hydroxide, MnO(OH)) and brucite (magnesium hydroxide, $Mg(OH)_2$). Hematite has been previously reported to exhibit two major Raman peaks under 532 nm excitation that fall within SHERLOC's detectable spectral range: a narrow peak at 400 cm^{-1} and a broad resonant peak at ~1320 cm^{-1} [Wang et al., 2004]. However, we could not resolve any Raman peaks from powdered hematite under DUV excitation, only the peaks of atmospheric O_2 and N_2. This is consistent with our observations that Fe-rich minerals tend to be strong UV absorbers, reducing the penetration of incident laser light as well as attenuating any Raman-scattered light [Shkolyar et al., 2018; Carrier et al., 2019; Razzell Hollis et al., 2020]. By contrast, the manganite rock sample exhibited a single detectable peak at 465 cm^{-1}, but this peak does not correlate to any known peak of manganite and is likely an indication of a minor quartz component in the rock. Manganite also exhibited a very weak peak at ~1564 cm^{-1}, probably from organic contamination. Brucite produced a single well-defined peak at 3653 cm^{-1} that we assigned to the Mg–OH hydroxyl stretching mode, but no detectable peaks at lower frequencies.

Silicates. Sixteen different silicate minerals were measured, including members of the K-feldspar, olivine, plagioclase, pyroxene, and silica groups, plus basaltic glass. The full list of minerals was as follows: albite, augite, bytownite, diopside, enstatite, epidote, fayalite, forsterite, hedenbergite, labradorite, microcline, olivine, opal, orthoclase, quartz, and topaz. Their spectra are shown in Fig. 9. Ten phyllosilicates were also measured, but these will be described in the following subsection. The silicate minerals generally show far weaker Raman scattering than the carbonate, sulfate, or borate minerals described earlier, as demonstrated by the relative intensity of the atmospheric N_2 peak at ~2330 cm^{-1} and, to a lesser extent, the O_2 peak at ~1560 cm^{-1}, for most spectra shown in Fig. 9. Weaker Raman scattering is a direct result of the silicate Si–O bonds being less polarizable than the more electron-rich bonds of carbonate, phosphate and sulfate [Griffith, 1969].

Despite lower signal yields, we were still able to detect very distinctive Raman peaks for key silicate minerals of significance to Martian geology, including quartz and olivine. Quartz was the most detectable silicate we studied, dominated by a strong narrow peak at 474–477 cm^{-1} that was easily detected despite being in the region that is significantly

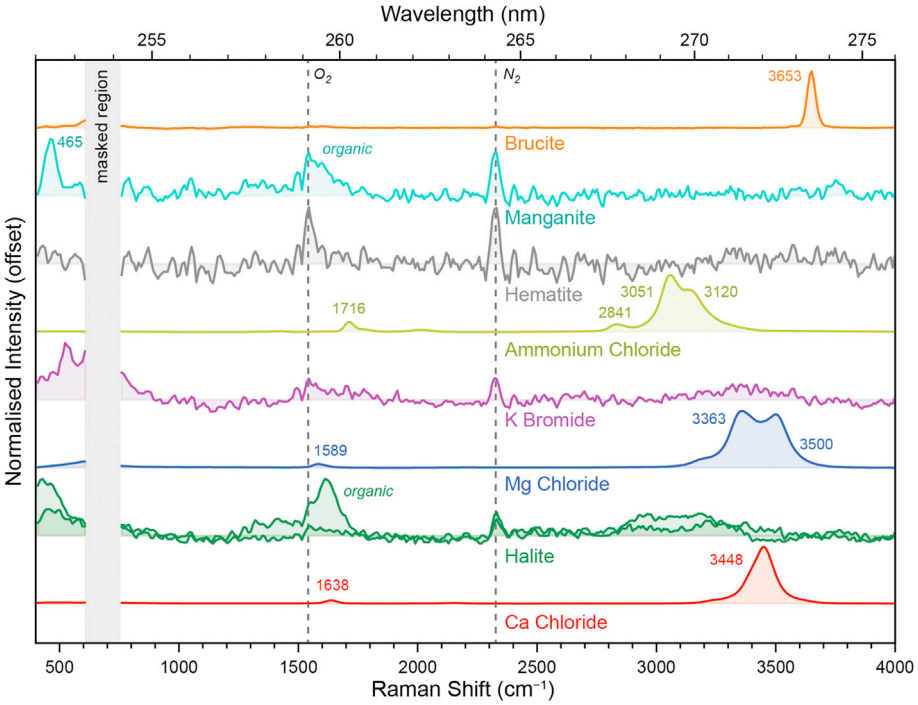

Fig. 8. DUV Raman spectra for various halide, metal oxide and metal hydroxide mineral samples, measured under Earth ambient conditions. See Fig. 4 for a summary of acquisition parameters and spectral processing.

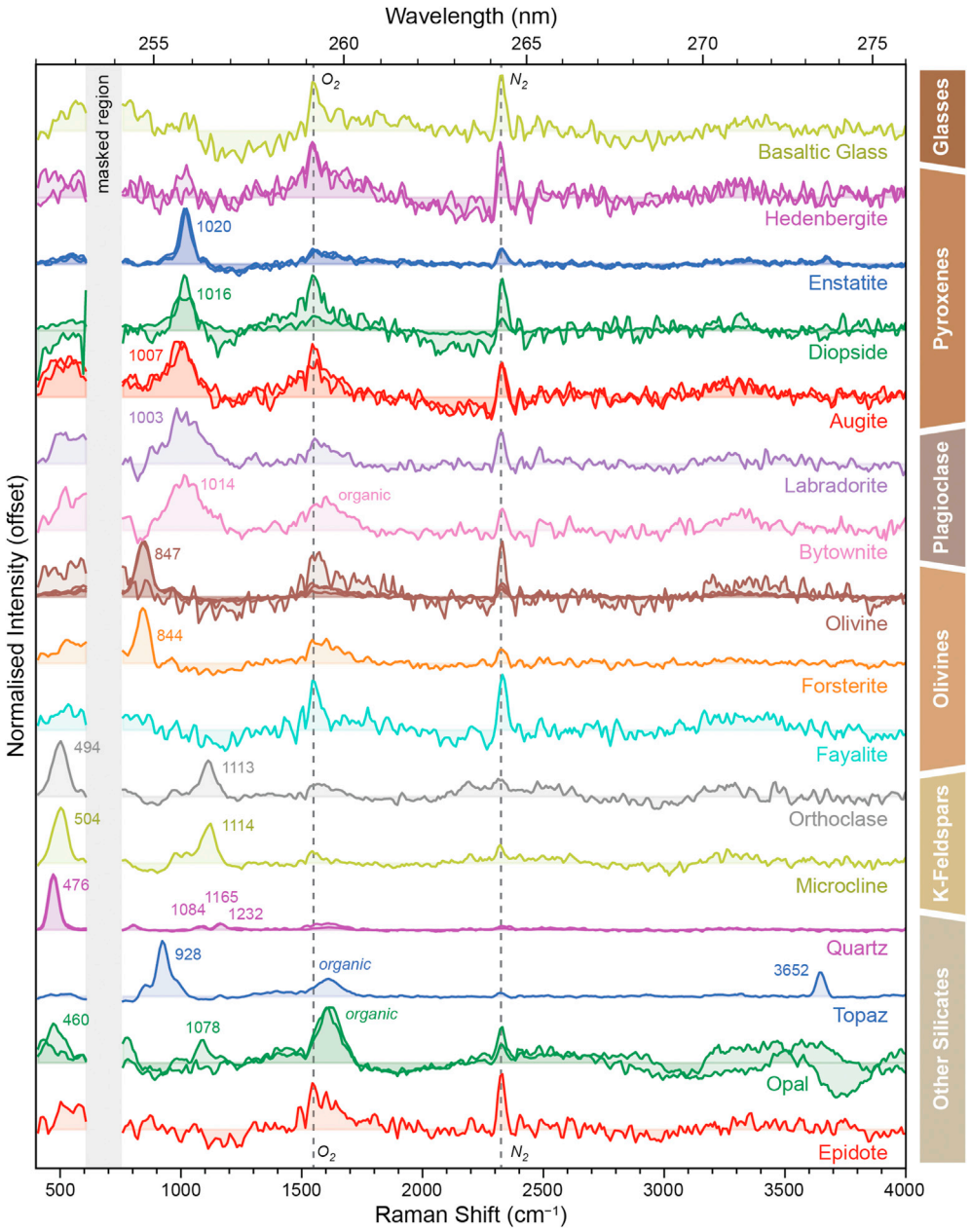

Fig. 9. DUV Raman spectra for various silicate mineral samples and basaltic glass, measured under Earth ambient conditions. See Fig. 4 for a summary of acquisition parameters and spectral processing.

attenuated by the instrument's edge filter (300–600 cm^{-1}). We estimate that the measured intensity of the 475 cm^{-1} peak was only ~10% of its true signal, based on the filter's transmittance at the corresponding wavelength (251.55 nm), and note that this peak exhibited the largest discrepancy (+9 cm^{-1}) with respect to its reported position in literature due to the reduced accuracy of our spectral calibration in the edge-filtered region. Quartz samples also exhibited some comparatively weak, but still detectable, peaks in the unfiltered region: a single peak at 805 cm^{-1} and a triplet of minor modes at 1084, 1166, and 1232 cm^{-1}, with the 1166 cm^{-1} peak being the strongest in the triplet and the 1232 cm^{-1} peak the weakest. Olivine and most other silicates were detectable via Raman peaks in the unfiltered region, typically at ~850 or ~1100 cm^{-1}. Of the silicate samples we investigated, the only major outlier was albite, which produced such strong fluorescence in the 250–300 nm range such that no Raman peaks could be resolved due to signal saturation even at the lowest laser exposure (see Fig. S19); as such, it is not included in Fig. 9 for the sake of clarity. This intense fluorescence is most likely due to the presence of rare earth elements in the albite sample, but requires further investigation.

The assignment of specific peaks to individual vibrational modes of the covalent lattice is complicated by the dramatic variation in structure adopted by different silicate minerals, but in general, silicate peaks at 400–500 cm^{-1} can be considered bending modes of the [SiO_4] tetrahedron, akin to ν_2 and ν_4 in sulfate/phosphate, while peaks in the 800–1300 cm^{-1} region are stretching modes comparable to ν_1 and ν_3 [Krishnamurti, 1958; Griffith, 1969; Czaja et al., 2009]. Silicates from the same group tend to exhibit similar spectra, summarized below, with the Fe-rich endmembers of each group tending to be the hardest to detect due to UV absorption by octahedral Fe complexes.

The K-feldspar group minerals (microcline and orthoclase) appeared identical with spectra exhibiting two strong peaks at 494–504 and 1113–1114 cm^{-1}. Their similarity is a result of these minerals being triclinic and monoclinic polymorphs with the same formula, $KAlSi_3O_8$.

The plagioclase group minerals (bytownite and labradorite) did not exhibit any significant Raman peaks in the 400–4000 cm^{-1} range, the only feature was a very broad, poorly defined peak around 1000 cm^{-1} that may be an artifact of background subtraction rather than a real scattering feature. It is unclear why the plagioclase minerals were undetectable, considering they have no appreciable Fe content, but plagioclase minerals have been reported to exhibit Raman spectra similar to K-feldspars under visible excitation [Freeman et al., 2008].

The pyroxene group minerals (augite, diopside, enstatite, and hedenbergite) were typified by a single relatively broad but well-defined peak with a maximum at 1000–1026 cm^{-1}, which was hardest to resolve in the Fe-endmember hedenbergite. This peak coincides with the reported positions of a pyroxene doublet at ~1010 and ~1030 cm^{-1} under visible excitation [Wang et al., 2001]. Although we are able to identify individual peak positions to within ~5 cm^{-1}, the nature of the doublet as two overlapping peaks with a peak-to-peak separation considerably smaller than the Brassboard's spectral resolution (54 cm^{-1}) means that the doublet becomes convoluted, appearing in our measurements as a single broad peak centered at an intermediate position.

The olivine group minerals (the Mg and Fe endmembers forsterite and fayalite, plus four intermediate olivines between Fo1 and Fo90 [Buz and Ehlmann, 2017]) tended to exhibit a single well defined peak at 844–847 cm^{-1}, which was undetectable in the Fe-endmember fayalite or the Fo1 olivine (pellet 4). Similar to the pyroxene series, the ~846 cm^{-1} olivine peak is likely a convolution of the doublet reported at ~820 and ~850 cm^{-1} for olivines under visible excitation [Chopelas, 1991; Kuebler et al., 2006]. Although Kuebler et al. [2006] described a systematic relationship between the olivine doublet's intensity ratio and Mg/Fe composition, because our measurements cannot resolve the individual peaks of the doublet we were unable to measure the intensity ratio or compare it to composition. However, SHERLOC's spectral resolution is markedly better than the Brassboard's (40 cm^{-1} vs 54 cm^{-1}), and thus the doublet may be resolvable in SHERLOC spectra, allowing for analysis of olivine composition based on its intensity ratio.

The remaining silicate samples studied included basaltic glass, epidote, opal, and topaz. The basaltic glass and epidote samples did not exhibit any distinctive Raman peaks that could be detected by the Brassboard instrument, while topaz had a strong peak at ~929 cm^{-1} plus a relatively minor Si–OH peak at 3652 cm^{-1}. Of the two opal samples studied, only the ChemCam calibration pellet (mix12-O) exhibited Raman peaks that could be reliably attributed to vibrations of the silicate lattice (two relatively weak modes at ~485 and ~1078 cm^{-1}, similar to quartz), but both samples showed signs of some organic contamination as shown by a broad Raman peak at ~1610 cm^{-1}. Similar peaks at ~1610 cm^{-1} were also apparent at varying intensities for the calibration target pellets for quartz and topaz (mix4-O and mix21-O respectively) and the bytownite pellet (C16630), suggesting minor amounts of organic contamination were present in these pellets as well.

The spectra in Fig. 9 indicate that SHERLOC will be capable of detecting Raman scattering from some silicate minerals, although signal yields were generally much lower when compared to the carbonates, sulfates and phosphates. As such silicates might not be detectable during short-exposure SHERLOC activities like survey scans. We again observed that minerals enriched with Fe, such as hedenbergite and fayalite, are harder to detect, although we note the plagioclase silicates also could not be detected despite having little to no Fe present. The identification of specific silicate minerals based on the pattern and positions of detected peaks may be limited to differentiation at a group level, e.g. olivines versus pyroxenes, but further work to optimize observation conditions may be needed and SHERLOC's superior spectral resolution may allow for greater differentiation. Of the silicate groups that produced detectable Raman spectra, the olivines and quartz were the easiest to distinguish as their dominant peaks (~845 and ~476 cm^{-1} respectively) fall well outside the 900–1600 cm^{-1} region where other minerals exhibit strong peaks. As such they should still be identifiable even in complex, mixed samples that display multiple overlapping mineral signatures.

Phyllosilicates. Ten distinct phyllosilicate minerals were measured, including two serpentine group minerals (antigorite and serpentine); two mica group minerals (biotite and muscovite), five clay minerals (chlorite, illite, kaolinite, montmorillonite, smectite), plus serpentinite rock. Like the other silicates, phyllosilicates can exhibit a wide range of structures consisting of combinations of tetrahedral and octahedral silicate layers arranged into 2-dimensional sheets. The smectite samples we investigated were synthetic minerals of varying Al/Mg/Fe^{II}/Fe^{III} composition; samples A, G, H, and J were all exclusively Fe^{III}-bearing clays while samples K and N were predominantly Fe^{II}-bearing clays [Fox et al., 2021], but we note that their oxidation state may have been changed after approximately 1 year of storage under ambient conditions.

Fig. 10 shows that the majority of the phyllosilicates we studied exhibited few discernible Raman peaks between 400 and 4000 cm^{-1} and are primarily dominated by background noise and the ubiquitous peaks of atmospheric O_2 and N_2. The most common spectral signature of the phyllosilicate samples was an octahedral Si–OH hydroxyl stretching mode, which appeared as a relatively narrow peak between 3600 and 3700 cm^{-1}. The exact position of this peak is known to vary based on both overall structure and occupation of the octahedral site by different metallic cations [Wang et al., 2015]. Indeed, the OH position differed by 12 cm^{-1} between serpentine and antigorite but only 1 cm^{-1} between serpentinite rock and antigorite. The difference in position suggests the serpentine sample may be lizardite-rich serpentine, while the serpentinite rock may be primarily antigorite [Petriglieri et al., 2015; Tarling et al., 2018]. In most phyllosilicates the OH peak is actually a doublet with a relatively small separation (<50 cm^{-1}) below the resolution of the Brassboard, but in kaolinite the separation is sufficiently large (60–80 cm^{-1}) that the doublet can be resolved as two peaks at 3632 and 3696 cm^{-1}.

Other spectral features can be seen in Fig. 10: a peak was observed at 556 and 530 cm^{-1} for the biotite and muscovite crystal samples but could not be assigned to any reported modes for either mineral. As such, we cannot be certain that this peak is a real Raman peak from either biotite or muscovite and should not be used for identification. Organic material was also present in at least six samples, with a broad organic G band observed at 1580–1620 cm^{-1} for chlorite, kaolinite, montmorillonite, muscovite, serpentine, and serpentinite, appearing spectroscopically similar to kerogenous/refractory organic material. The preponderance of organic material is not unexpected, as these minerals are known to absorb organic material onto ultrafine particle surfaces and within structural interlayers, furthering the long-standing observation that phyllosilicate minerals have biosignature preservation potential and are considered high value targets for the *Mars 2020* mission [Ehlmann et al., 2008a; Fornaro et al., 2018; Beaty et al., 2019].

Part of the difficulty in detecting phyllosilicates is that the major peaks of the silicate structure itself have been reported to occur around 200–300 cm^{-1} and 600–800 cm^{-1} under visible excitation [Wang et al., 2015], two regions that are either outside of SHERLOC's spectral range or are obscured by the 252.93 nm laser emission line. However, this does not mean it is impossible to detect other Raman peaks of phyllosilicates under DUV excitation; an earlier study using a liquid-N_2 cooled DUV spectrometer reported that the synthetic smectite samples produced two detectable peaks at ~1050 and ~3600 cm^{-1}, the latter being an octahedral Si–OH hydroxyl mode [Fox et al., 2021]. Given that the SNR yield of a 25 point average on the Brassboard is roughly equivalent to a single point spectrum acquisition on SHERLOC, it may be possible to resolve phyllosilicate phases in SHERLOC maps through spatial averaging of multiple point spectra, provided that they are not intimately mixed with a strong Raman scatterer (such as gypsum) or a strong UV absorber (such as an Fe-rich mineral).

4. Conclusions

To assist SHERLOC data analysis during the *Mars 2020* mission and enable the identification of mineralogy using DUV Raman spectra, we

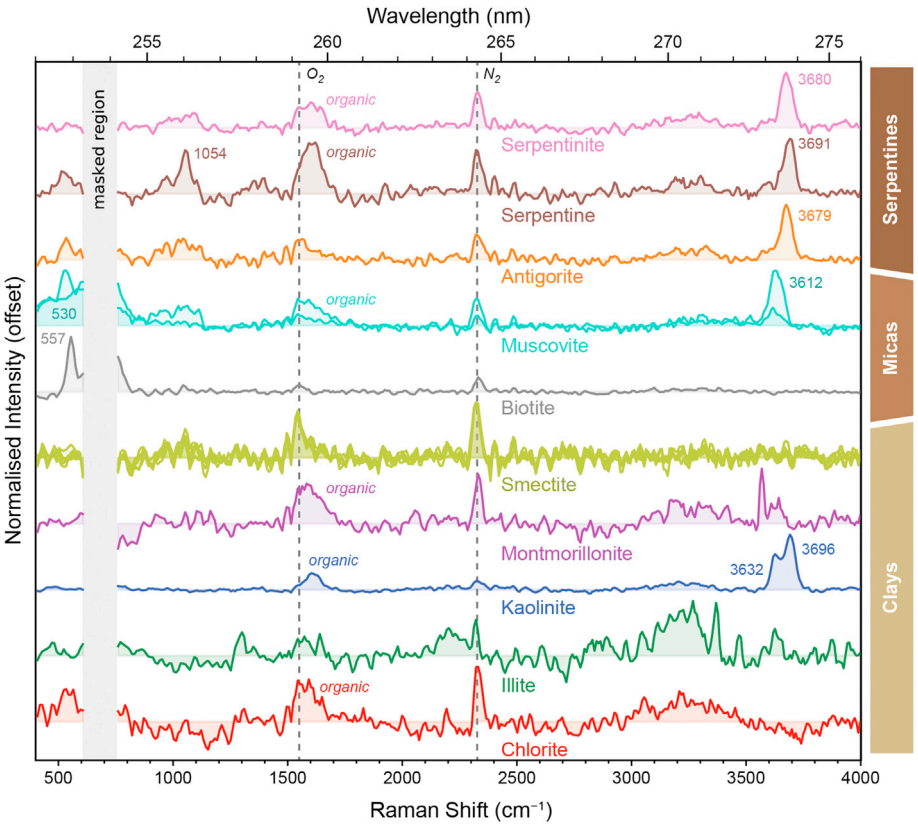

Fig. 10. DUV Raman spectra for various phyllosilicate mineral samples, averaged over 25 points at 800 laser pulses per point. See Fig. 4 for a summary of acquisition parameters and spectral processing.

have assembled a spectral library of mineral standards as measured by the Brassboard, an optical analog of the SHERLOC instrument. The Brassboard (and SHERLOC) is capable of detecting the internal vibrational modes of several key minerals that appear in particular spectral regions: major bending modes at 400–600 cm^{-1}, major stretching modes at 800–1200 cm^{-1}, and hydrate/hydroxide modes at 3000–3700 cm^{-1}, with all peak positions measured with an estimated uncertainty of ± 5 cm^{-1}. SHERLOC's more powerful laser and better optical throughput is expected to yield roughly 6x as much Raman scattering per laser pulse for any given sample. Consequently, there may be some minerals that exhibited no distinguishable Raman peaks in this study but may still be detectable to SHERLOC; the DUV Raman spectra we have described here should be considered a highly conservative estimation of how effectively SHERLOC can be used to detect and identify different minerals.

We have shown that SHERLOC is capable of detecting many minerals that are relevant to the geological history of Jezero crater, including borates, carbonates, sulfates, phosphates, halides, silicates and phyllosilicates. We found that carbonate, sulfate, and phosphate minerals tend to produce sufficient Raman scattering to be detectable at exposure energies as low as 20 μJ, comparable to a standard SHERLOC survey activity, which will maximize the scientific return from SHERLOC data and enable mapping of mineralogical composition over larger areas. Silicate and phyllosilicate minerals tend to yield less Raman scattering signal but the majority are still detectable at longer exposures of ~3000 μJ, comparable to laser output during a standard SHERLOC Detail Scan. We also noted that Fe-rich minerals tend to be harder to detect than Fe-poor minerals due to significant UV absorption, and therefore it appears that local Fe content may be a key factor in determining limits of detection on a sample by sample basis. This highlights the importance of interpreting SHERLOC data alongside information on elemental composition acquired from the Planetary Instrument for X-Ray Lithochemistry (PIXL) and other *Mars 2020* instruments.

SHERLOC is also capable of distinguishing different classes of minerals based on the rough position of the dominant (strongest) Raman peak and observation of any minor peaks (see Fig. 4). The specificity of Raman peaks to molecular vibrations means that minerals of the same class (e.g. carbonates) exhibit similar spectra, the observed peak positions may be used to distinguish similar minerals (e.g. calcite vs dolomite) provided that their dominant peak positions differ by at least ~10 cm^{-1}. Based on the spectra we have described, it should be possible to identify a number of important minerals using SHERLOC. By comparing data collected from SHERLOC to the spectra in this library, members of the *Mars 2020* science team and the wider scientific community will be better equipped to analyze and interpret the mineralogy of rocks investigated by the *Perseverance* rover during its mission and provide crucial context for collected/returned samples.

Author statement

Authors' Statement for "A Deep-Ultraviolet Raman and Fluorescence Spectral Library of 62 Minerals for the SHERLOC instrument onboard Mars 2020"

The authors declare that this manuscript is original, has not been published before and is not currently being considered for publication elsewhere.

We confirm that the manuscript has been read and approved by all named authors and that there are no other persons who satisfied the criteria for authorship but are not listed. We further confirm that the order of authors listed in the manuscript has been approved by all of us.

We understand that the Corresponding Author is the sole contact for the Editorial process. He/she is responsible for communicating with the other authors about progress, submissions of revisions and final approval of proofs.

Declaration of competing interest

The authors declare that they have no known competing financial interests or personal relationships that could have appeared to influence the work reported in this paper.

Acknowledgements

The research was carried out at the Jet Propulsion Laboratory, California Institute of Technology, under a contract with the National Aeronautics and Space Administration (80NM0018D0004). Government sponsorship acknowledged. © 2021, all rights reserved. We would like to thank Sandy Asher, Adrian Brown, Ken Edgett, Svetlana Shkolyar, Andrew Steele, and Anastasia Yanchilina for helpful discussions and comments.

Appendix A. Supplementary data

Supplementary data to this article can be found online at https://doi.org/10.1016/j.pss.2021.105356.

References

Abbey, W.J., Bhartia, R., Beegle, L.W., Deflores, L., Paez, V., Sijapati, K., et al., 2017. Deep UV Raman spectroscopy for planetary exploration: the search for in situ organics. Icarus 290, 201–214. https://doi.org/10.1016/j.icarus.2017.01.039.

Adler, H.H., Kerr, P.F., 1963. Infrared absorption frequency trends for anhydrous normal carbonates. Am. Mineral. 48, 124–137.

Asher, S.A., 1984. Ultraviolet resonance Raman spectrometry for detection and speciation of trace polycyclic aromatic hydrocarbons. Anal. Chem. 56, 720–724. https://doi.org/10.1021/ac00268a029.

Asher, S.A., 1993. UV resonance Raman spectroscopy for analytical, physical, and biophysical chemistry. Anal. Chem. 65, 201A–210A. https://doi.org/10.1021/ac00052a715.

Beaty, D.W., Grady, M.M., McSween, H.Y., Sefton-Nash, E., Carrier, B.L., Altieri, F., et al., 2019. The potential science and engineering value of samples delivered to Earth by Mars sample return: international MSR Objectives and Samples Team (iMOST). Meteoritics Planet Sci. 54, S3–S152. https://doi.org/10.1111/maps.13242.

Beegle, L., Bhartia, R., White, M., Deflores, L., Abbey, W., Wu, Y.H., et al., 2015. SHERLOC: scanning habitable environments with Raman & luminescence for organics & chemicals. IEEE Aerospace Conference Proceedings. https://doi.org/10.1109/AERO.2015.7119105.

Bhartia, R., Hug, W.F., Reid, R.D., 2012. Improved sensing using simultaneous deep UV Raman and fluorescence detection. Chem. Biol. Radiol. Nucl. Explos. Sens. XIII 8358 (9), 83581A. https://doi.org/10.1117/12.920170, 83581A.

Bhartia, R., Beegle, L.W., DeFlores, L., et al., 2021. Perseverance's scanning habitable environments with Raman and luminescence for organics and chemicals (SHERLOC) investigation. Space Sci. Rev. (in press).

Bischoff, W.D., Sharma, S.K., Mackenzie, F.T., 1985. Carbonate ion disorder in synthetic and biogenic magnesium calcites : a Raman spectral study. Am. Mineral. 70, 581–589.

Brotton, S.J., Kaiser, R.I., 2013. In situ Raman spectroscopic study of gypsum ($CaSO_4 \cdot 2H_2O$) and epsomite ($MgSO_4 \cdot 7H_2O$) dehydration utilizing an ultrasonic levitator. J. Phys. Chem. Lett. 4, 669–673. https://doi.org/10.1021/jz301861a.

Brown, A.J., Viviano, C.E., Goudge, T.A., 2020. Olivine-carbonate mineralogy of the Jezero crater region. J. Geophys. Res. Planets 125. https://doi.org/10.1029/2019JE006011.

Buz, J., Ehlmann, B.L., 2017. The effect of grain size on the VIS-SWIR spectrum of olivines: an exploration of standard, modified and exponential Gaussians for determination of crystal chemistry. Lunar Planet. Sci. Conf. 3027, 2017.

Carrier, B.L., Abbey, W.J., Beegle, L.W., Bhartia, R., Liu, Y., 2019. Attenuation of ultraviolet radiation in rocks and minerals: implications for Mars science. J. Geophys. Res. Planets 124, 2599–2612. https://doi.org/10.1029/2018JE005758.

Chan, Q.H.S., Zolensky, M.E., Bodnar, R.J., Farley, C., Cheung, J.C.H., 2017. Investigation of organo-carbonate associations in carbonaceous chondrites by Raman spectroscopy. Geochem. Cosmochim. Acta 201, 392–409. https://doi.org/10.1016/j.gca.2016.10.048.

Chopelas, A., 1991. Single crystal Raman spectra of forsterite, fayalite, and monticellite. Am. Mineral. 76, 1101–1109.

Czaja, A.D., Kudryavtsev, A.B., Cody, G.D., Schopf, J.W., 2009. Characterization of permineralized kerogen from an Eocene fossil fern. Org. Geochem. 40, 353–364. https://doi.org/10.1016/j.orggeochem.2008.12.002.

De La Pierre, M., Carteret, C., Maschio, L., André, E., Orlando, R., Dovesi, R., 2014. The Raman spectrum of $CaCO_3$ polymorphs calcite and aragonite : a combined experimental and computational study. J. Chem. Phys. 140, 164509. https://doi.org/10.1063/1.4871900.

Ehlmann, B.L., Mustard, J.F., Fassett, C.I., Schon, S.C., Head, J.W., Des Marais, D.J., Grant, J.A., Murchie, S.L., 2008a. Clay minerals in delta deposits and organic preservation potential on Mars. Nat. Geosci. 1, 355–358. https://doi.org/10.1038/ngeo207.

Ehlmann, B.L., Mustard, J.F., Murchie, S.L., Poulet, F., Bishop, J.L., Brown, A.J., et al., 2008b. Orbital identification of carbonate-bearing rocks on Mars. Science 80 (322), 1828–1833. https://doi.org/10.1126/science.1164759.

Ehlmann, B.L., et al., 2009. Identification of hydrated silicate minerals on Mars using MRO-CRISM: geologic context near Nili Fossae and implications for aqueous alteration. J. Geophys. Res. 114, E00D08. https://doi.org/10.1029/2009JE003339.

Ehlmann, B.L., 2010. Early Mars environments revealed through near-infrared spectroscopy of alteration minerals. PhD. https://doi.org/10.7301/Z0QN650G.

Ehlmann, B.L., Mustard, J.F., Murchie, S.L., Bibring, J.P., Meunier, A., Fraeman, A.A., et al., 2011. Subsurface water and clay mineral formation during the early history of Mars. Nature 479, 53–60. https://doi.org/10.1038/nature10582.

Eshelman, E.J., Malaska, M.J., Manatt, K.S., Doloboff, I.J., Wanger, G., Willis, M.C., et al., 2019. WATSON: in situ organic detection in subsurface ice using deep-UV fluorescence spectroscopy. Astrobiology 19, 771–784. https://doi.org/10.1089/ast.2018.1925.

Farley, K.A., Williford, K.H., Stack, K.M., Bhartia, R., Chen, A., de la Torre, M., et al., 2020. Mars 2020 mission overview. Space Sci. Rev. 216. https://doi.org/10.1007/s11214-020-00762-y.

Fassett, C.I., Head III, J.W., 2005. Fluvial sedimentary deposits on Mars: ancient deltas in a crater lake in the Nili Fossae region. Geophys. Res. Lett. 32, L14201. https://doi.org/10.1029/2005GL023456.

Fornaro, T., Steele, A., Brucato, J., 2018. Catalytic/protective properties of martian minerals and implications for possible origin of life on Mars. Life 8, 56. https://doi.org/10.3390/life8040056.

Fox, V., Kupper, R.J., Ehlmann, B.E., Catalano, J.G., Razzell Hollis, J., Abbey, W.J., et al., 2021. Synthesis and characterization of Fe(III)-Fe(II)-Mg-Al smectite solid solutions and implications for planetary science. Am. Mineral. (in press).

Freeman, J.J., Wang, A., Kuebler, K.E., Jolliff, B.L., Haskin, L.A., 2008. Characterization of natural feldspars by Raman spectroscopy for future planetary exploration. Can. Mineral. 46, 1477–1500. https://doi.org/10.3749/canmin.46.6.1477.

Frost, R.L., Xi, Y., Scholz, R., Maria Belotti, F., Cândido Filho, M., 2013. Infrared and Raman spectroscopic characterization of the borate mineral colemanite – $CaB_3O_4(OH)_3.H_2O$ – implications for the molecular structure. J. Mol. Struct. 1037, 23–28. https://doi.org/10.1016/j.molstruc.2012.11.047.

Goudge, T.A., Mustard, J.F., Head, J.W., Fassett, C.I., Wiseman, S.M., 2015. Assessing the mineralogy of the watershed and fan deposits of the Jezero Crater paleolake system, Mars. J. Geophys. Res. Planets 120, 775–808. https://doi.org/10.1002/2014JE004782.

Goudge, T.A., Milliken, R.E., Head, J.W., Mustard, J.F., Fassett, C.I., 2017. Sedimentological evidence for a deltaic origin of the western fan deposit in Jezero crater, Mars and implications for future exploration. Earth Planet Sci. Lett. 458, 357–365. https://doi.org/10.1016/j.epsl.2016.10.056.

Griffith, W.P., 1969. Raman spectroscopy of minerals. Nature 224, 264–266.

Gunasekaran, S., Anbalagan, G., Pandi, S., 2006. Raman and infrared spectra of carbonates of calcite structure. J. Raman Spectrosc. 37, 892–899. https://doi.org/10.1002/jrs.1518.

Hays, L.E., Graham, H.V., Des Marais, D.J., Hausrath, E.M., Horgan, B., McCollom, T.M., et al., 2017. Biosignature preservation and detection in Mars analog environments. Astrobiology 17, 363–400. https://doi.org/10.1089/ast.2016.1627.

Horgan, B.H.N., Anderson, R.B., Dromart, G., Amador, E.S., Rice, M.S., 2020. The mineral diversity of Jezero crater: evidence for possible lacustrine carbonates on Mars. Icarus 339, 113526. https://doi.org/10.1016/j.icarus.2019.113526.

Jones, E., Oliphant, E., Peterson, P., et al., 2001. SciPy: open source scientific tools for Python. Available at: http://www.scipy.org/. (Accessed 20 July 2018). Accessed.

Kaabar, W., Bott, S., Devonshire, R., 2011. Raman spectroscopic study of mixed carbonate materials. Spectrochim. Acta Part A Mol. Biomol. Spectrosc. 78, 136–141. https://doi.org/10.1016/j.saa.2010.09.011.

Kloprogge, J.T., Frost, R.L., 1999. Raman microscopic study of some borate minerals: ulexite, kernite, and inderite. Appl. Spectrosc. 53, 356–364.

Krishnamurti, D., 1958. The Raman spectrum of quartz and its interpretation. Proc. Indian Acad. Sci. Sect. A 47, 276–291.

Krishnan, R.S., 1947. Raman spectrum of ammonium chloride and its variation with temperature. Proc. Indian Acad. Sci. Sect. A 26, 432–449. https://doi.org/10.1007/BF03170900.

Kuebler, K.E., Jolliff, B.L., Wang, A., Haskin, L.A., 2006. Extracting olivine (Fo-Fa) compositions from Raman spectral peak positions. Geochem. Cosmochim. Acta 70, 6201–6222. https://doi.org/10.1016/j.gca.2006.07.035.

Litasov, K.D., Podgornykh, N.M., 2017. Raman spectroscopy of various phosphate minerals and occurrence of tuite in the Elga IIE iron meteorite. J. Raman Spectrosc. 48, 1518–1527. https://doi.org/10.1002/jrs.5119.

Long, D.A., 1977. Raman Spectroscopy. McGraw Hill, London.

Mabrouk, K. Ben, Kauffmann, T.H., Aroui, H., Fontana, M.D., 2013. Raman study of cation effect on sulfate vibration modes in solid state and in aqueous solutions. J. Raman Spectrosc. 44, 1603–1608.

Martin, P.E., Ehlmann, B.L., Thomas, N.H., Wiens, R.C., Razzell Hollis, J., Beegle, L.W., et al., 2020. Studies of a lacustrine-volcanic Mars analog field site with mars-2020-like instruments. Earth Sp. Sci. 7, 1–28. https://doi.org/10.1029/2019EA000720.

McCollom, T.M., Ehlmann, B.L., Wang, A., Hynek, B.M., Moskowitz, B., Berquó, T.S., 2014. Detection of iron substitution in natroalunite-natrojarosite solid solutions and potential implications for Mars. Am. Mineral. 99, 948–964. https://doi.org/10.2138/am.2014.4617.

McLennan, S.M., et al., MEPAG E2E-iSAG, 2011. Planning for Mars Returned Sample Science: Final report of the MSR End-to-End International Science Analysis Group (E2E-iSAG). Astrobiology 12, 175–230.

Montagnac, G., Caracas, R., Bobocioiu, E., Vittoz, F., Reynard, B., 2013. Anharmonicity of graphite from UV Raman spectroscopy to 2700 K. Carbon 54, 68–75. https://doi.org/10.1016/j.carbon.2012.11.004.

Murchie, S.L., Mustard, J.F., Ehlmann, B.L., Milliken, R.E., Bishop, J.L., McKeown, N.K., et al., 2009. A synthesis of Martian aqueous mineralogy after 1 Mars year of observations from the Mars Reconnaissance Orbiter. J. Geophys. Res. E Planets 114, 1–30. https://doi.org/10.1029/2009JE003342.

Mustard, J., Adler, M., Allwood, A., Bass, D., Beaty, D., Bell, J., et al., 2013. Report of the Mars 2020 science definition team. In: Mars Explor. Progr. Anal. Gr, pp. 155–205. Available at: http://mepag.jpl.nasa.gov/reports/MEP/Mars_2020_SDT_Report_Appendix.pdf.

Newville, M., Stensitzki, T., Allen, D.B., Ingargiola, A., 2014. LMFIT: non- linear least-square minimization and curve-fitting for Python. Available at: https://lmfit.github.io/lmfit-py/index.html. (Accessed 10 March 2018). Accessed.

Petriglieri, J.R., Salvioli-Mariani, E., Mantovani, L., Tribaudino, M., Lottici, P.P., Laporte-Magoni, C., et al., 2015. Micro-Raman mapping of the polymorphs of serpentine. J. Raman Spectrosc. 46, 953–958. https://doi.org/10.1002/jrs.4695.

Razzell Hollis, J., Rheingold, D., Bhartia, R., Beegle, L.W., 2020. An optical model for quantitative Raman microspectroscopy. Appl. Spectrosc. 74, 684–700. https://doi.org/10.1177/0003702819895299.

Razzell Hollis, J., Ireland, S., Abbey, W., Bhartia, R., Beegle, L.W., 2021a. Deep-ultraviolet Raman spectra of Mars-relevant evaporite minerals under 248.6 nm excitation. Icarus 357, 114067. https://doi.org/10.1016/j.icarus.2020.114067.

Razzell Hollis, J., Fornaro, T., Rapin, W., Wade, J., Vicente-Retortillo, Á., Steele, A., et al., 2021b. Detection and Degradation of Adenosine Monophosphate in Perchlorate-Spiked Martian Regolith Analogue. In: Deep-Ultraviolet Spectroscopy. Astrobiology (in press).

Rossman, G.R., Ehlmann, B.L., 2019. Electronic spectra of minerals in the visible and near-infrared regions. In: Bishop, J.L., Bell, J.F., Moersch, J. (Eds.), Remote Compositional Analysis. Cambridge University Press. https://doi.org/10.1017/9781316888872.

Scheller, E.L., Ehlmann, B.L., 2020. Composition, stratigraphy, and geological history of the noachian basement surrounding the Isidis impact basin. J. Geophys. Res. Planets 125. https://doi.org/10.1029/2019JE006190.

Schon, S.C., Head, J.W., Fassett, C.I., 2012. An overfilled lacustrine system and progradational delta in Jezero crater, Mars: implications for Noachian climate. Planet. Space Sci. 67, 28–45. https://doi.org/10.1016/j.pss.2012.02.003.

Schopf, J.W., Kudryavtsev, A.B., Agresti, D.G., Czaja, A.D., Wdowiak, T.J., 2005. Raman imagery: a new approach to assess the geochemical maturity and biogenicity of permineralized precambrian fossils. Astrobiology 5, 333–371.

Shkolyar, S., Eshelman, E.J., Farmer, J.D., Hamilton, D., Daly, M.G., Youngbull, C., 2018. Detecting kerogen as a biosignature using colocated UV time-gated Raman and fluorescence spectroscopy. Astrobiology 18, 431–454. https://doi.org/10.1089/ast.2017.1716.

Shkolyar, S., Lalla, E., Konstantindis, M., Cote, K., Daly, M.G., Steele, A., 2021. Detecting Ce^{3+} as a biosignature mimicker using UV time-resolved laser-induced fluorescence and Raman spectroscopy: implications for planetary missions. Icarus 354, 114093. https://doi.org/10.1016/j.icarus.2020.114093.

Stack, K.M., et al., 2020. Photogeologic map of the perseverance rover field site in Jezero crater constructed by the Mars 2020 science team. Space Sci. Rev. 216, 127. https://doi.org/10.1007/s11214-020-00739-x.

Steele, A., McCubbin, F.M., Fries, M.D., 2016. The provenance, formation, and implications of reduced carbon phases in Martian meteorites. Meteoritics Planet Sci. 51, 2203–2225. https://doi.org/10.1111/maps.12670.

Tarcea, N., Frosch, T., Rösch, P., Hilchenbach, M., Stuffler, T., Hofer, S., et al., 2008. Raman spectroscopy - a powerful tool for in situ planetary science. Space Sci. Rev. 135, 281–292. https://doi.org/10.1007/s11214-007-9279-y.

Tarling, M.S., Rooney, J.S., Viti, C., Smith, S.A.F., Gordon, K.C., 2018. Distinguishing the Raman spectrum of polygonal serpentine. J. Raman Spectrosc. 49, 1978–1984. https://doi.org/10.1002/jrs.5475.

Thomas, N.H., Ehlmann, B.L., Anderson, D.E., Clegg, S.M., Forni, O., Schröder, S., et al., 2018. Characterization of hydrogen in basaltic materials with laser-induced breakdown spectroscopy (LIBS) for application to MSL ChemCam data. J. Geophys. Res. Planets 123, 1996–2021. https://doi.org/10.1029/2017JE005467.

Uckert, K., Bhartia, R., Michel, J., 2019. A semi-autonomous method to detect cosmic rays in Raman hyperspectral data sets. Appl. Spectrosc. 73, 1019–1027. https://doi.org/10.1177/0003702819850584.

Uckert, K., Bhartia, R., Beegle, L.W., Monacelli, B., Asher, S.A., Burton, A., et al., 2021. Calibration of the SHERLOC deep UV fluorescence/Raman spectrometer on the Perseverance Rover. Appl. Spectrosc. (in press).

van der Walt, S., Colbert, S.C., Varoquaux, G., 2011. The NumPy array: a structure for efficient numerical computation. Comput. Sci. Eng. 13, 22–30. https://doi.org/10.1109/MCSE.2011.37.

Wang, A., Jolliff, B.L., Haskin, L.A., Kuebler, K.E., Viskupic, K.M., 2001. Characterization and comparison of structural and compositional features of planetary quadrilateral pyroxenes by Raman spectroscopy. Am. Mineral. 86, 790–806. https://doi.org/10.2138/am-2001-0703.

Wang, A., Kuebler, K., Jolliff, B., Haskin, L.A., 2004. Mineralogy of a Martian meteorite as determined by Raman spectroscopy. J. Raman Spectrosc. 35, 504–514. https://doi.org/10.1002/jrs.1175.

Wang, A., Freeman, J.J., Jolliff, B.L., Chou, I.M., 2006. Sulfates on Mars: a systematic Raman spectroscopic study of hydration states of magnesium sulfates. Geochem. Cosmochim. Acta 70, 6118–6135. https://doi.org/10.1016/j.gca.2006.05.022.

Wang, A., Freeman, J.J., Jolliff, B.L., 2015. Understanding the Raman spectral features of phyllosilicates. J. Raman Spectrosc. 46, 829–845. https://doi.org/10.1002/jrs.4680.

Williford, K.H., Farley, K.A., Stack, K.M., Allwood, A.C., Beaty, D., Beegle, L.W., et al., 2018. In: Cabrol, N.A., Grin, E.A. (Eds.), "Chapter 11 - the NASA Mars 2020 Rover Mission and the Search for Extraterrestrial Life," in *from Habitability to Life on Mars*. Elsevier, pp. 275–308. https://doi.org/10.1016/B978-0-12-809935-3.00010-4.